“Numerical modeling of the mechanical behaviour of an osteon with microcracks”

Authors: Eugenio Giner, Camila Arango, Ana Vercher, F. Javier Fuenmayor

HIGHLIGHTS:

- Two strategies for the FE modeling of microdamage within an osteon are presented
- A failure criteria for delamination in composites is applied (Brewer and Lagacé)
- Elastic properties take into account the orientation of fibrils in each lamella
- Good agreement with experimental evidence reported by other authors is attained
- Interlaminar shear stresses dominate failure under compressive diametral load

Numerical modeling of the mechanical behaviour of an osteon with microcracks

Eugenio Giner*, Camila Arango, Ana Vercher, F. Javier Fuenmayor

Dept. de Ingeniería Mecánica y de Materiales - CITV,
Universitat Politècnica de València, Camino de Vera, 46022 Valencia, Spain.

Abstract

In this work, we present two strategies for the numerical modeling of microcracks and damage within an osteon. A numerical model of a single osteon under compressive diametral load is developed, including lamellae organized concentrically around the haversian canal and the presence of lacunae. Elastic properties have been estimated from micromechanical models that consider the mineralized collagen fibrils reinforced with hydroxyapatite crystals and the dominating orientation of the fibrils in each lamella. Microcracks are simulated through the node release technique, enabling propagation along the lamellae interfaces by application of failure criteria initially conceived for composite materials, in particular the Brewer and Lagacé criterion for delamination. A second approach is also presented, which is based on the progressive degradation of the stiffness at the element level as the damage increases. Both strategies are discussed, showing a good agreement with experimental evidence reported by other authors. It is concluded that interlaminar shear stresses are the main cause of failure of an osteon under compressive diametral load.

Keywords: Cortical bone, microcracks, finite element method

*Corresponding author. Tel.: +34-96-3877007 ext. 76218; fax: +34-96-3877629.
Email address: eginerm@mcm.upv.es (Eugenio Giner)

1. INTRODUCTION

From a structural viewpoint, cortical bone tissue can be considered as a composite material hierarchically structured at different scales, see e.g. Cowin (2001); Rho et al. (1998); Taylor et al. (2007). At the nanostructural level (about 10–10^2 nm) is formed by type I collagen fibrils, other organic substances (mainly proteins) and a mineral phase of hydroxyapatite, HA, (Rho et al., 1998; Ritchie et al., 2005). At the microstructural scale (between 1–10^3 μm), mineralized collagen fibrils are grouped together within interfibrillar matrix in lamellar structures that are about 3–7 μm thick. These lamellae are arranged concentrically around the haversian canal, forming the secondary osteons (see Fig. 1), which are the basic microstructural unit of the cortical bone tissue and whose diameter ranges from 50 to 500 μm. A less organized structure with a high mineral content is found in the interstitial matrix filling the space among osteons. The interstitial matrix is in fact remaining tissue associated with old osteons. The microstructural level constitutes the working scale of this study, as the analysis is focused on the mechanical behaviour of a single osteon. There exist other morphological elements at this microstructural level (Rho et al., 1998; Ritchie et al., 2005): the haversian canal; the cement line, i.e. the outer osteon boundary of about 1 μm thick (Prendergast and Huiskes, 1996); the lacunae, located mainly between lamellae and that contain the osteocytes, and the Volkmann canals that connect transversally the haversian canals. There is also a very fine network of canaliculi that connect the osteocytes, the so-called synctycium (Taylor et al., 2007). Some of these morphological elements will not be included in the numerical model here presented, since it is deemed that their relevance in the mechanical behavior at the micro scale is secondary.

There is consensus in the literature (Taylor et al., 2007; Vashishth, 2007; Yang et al., 2006) regarding the two basic microdamage modes that can be found in cortical bone tissue: on one hand, the existence of microcracks (about $50 - 200$ μm long) and, on the other hand, the presence of diffuse damage zones, associated with a lower hierarchical scale, at the collagen fibril levels. The mechanisms that relate the fracture risk level and the microdamage level are not yet well defined, but it is clear the relationship between the microdamage levels and the reduction of the tissue fracture toughness (Yang et al., 2006). It is also well known the essential role played by the microdamage level in activating the remodelling process (Taylor et al., 2007; Ritchie et al., 2005; Taylor, 2007; Martínez-Reina et al., 2009). Therefore, the analysis of these mechanisms is of especial relevance.

In this work, we follow a mechanistic approach (Taylor et al., 2007) to study bone microdamage. This approach takes into consideration the microstructural details for a better understanding of the microdamage processes (Ritchie et al., 2005; Nalla et al., 2003). The numerical models developed in this work aim at presenting strategies for analyzing the mechanical behaviour of cortical tissue in presence of microcracks.

The objective of the work is to present two numerical approaches (the node release technique and the progressive damage approach) to simulate the experimentally observed behaviour reported by other authors. The aim of the analysis is to simulate the experimental work carried out by Ascenzi and Bonucci in single osteons at the microscale (Ascenzi et al., 1973) and other more recent experimental results reported by Ebacher and Wang (2009); Ebacher et al. (2012). More precisely, the behaviour of a single osteon under transverse compressive loading is modelled, i.e. compressive loading in radial direction of the osteon. Both Ascenzi et al. (1973) and Ebacher et al. (2012) observed that circumferential microcracks appear in those lamellae whose fibrils are aligned in the axial direction of the osteon. In Section 2, we give a brief description of the tests performed by Ascenzi et al. (1973) and the damage observed by Ascenzi et al. (1973) and Ebacher et al. (2012). In order to define the numerical model, it is necessary to provide a characterization of the elastic and strength properties of the tissue at this scale, as detailed in Sections 3 and 4, respectively. The numerical model analyzed with the finite element code Abaqus^{TM} (2012) is described in Section 5, along with the two techniques proposed for modeling the microdamage behavior in Section 6: a node-release technique (NRT) to simulate advancing microcracks and a progressive damage approach. Both approaches are compared and correlated with the experimental evidence in Section 7. The analyses show that the main cause of failure under compressive diametral load is the existence of interlaminar shear stresses that lead to lamellae separation.

2. STRENGTH BEHAVIOR OF AN OSTEON UNDER COMPRESSIVE RADIAL LOADING

Ascenzi et al. (1973) proposed an experimental setting for studying the strength behavior of an osteon and its lamellae under compressive radial loads. The sketch in Fig. 2 shows the simple configuration used, in which a section of an osteon (30-40 μm thick) is placed on a slide and pressed against the side of a coverslip (160 μm thick) using a spatula, thus being subjected to radial loading.

Ascenzi et al. (1973) gave detailed indications about the experimental procedure. In a previous work, Ascenzi and Bonucci (1968) also described the procedure followed to extract microsamples of single osteons from cortical tissue. The tissue corresponded to the diaphysis of human femurs of different ages (between 18 and 31 years old) with no apparent skeletal defects. The number of samples was sixty and the samples were kept wet by hydration with saline solution. Due to the sample extracting procedure, the osteon geometry can be assumed to be cylindrical in practice. In fact, Ascenzi et al. (1973) selected those osteons whose geometry was essentially circular on a transverse plane.

We will focus on the dominant type of osteon that can be found in the cortical tissue of long bones, named type I in Ascenzi et al. (1973). Its main feature is an alternated lamellar arrangement, sketched in Fig. 3: lamellae with fibrils essentially aligned in the axial direction of the osteon alternated with lamellae whose fibrils are mainly aligned in the circumferential direction. Hence, fibrils in one lamella make an angle of nearly 90° with the fibrils in the next. Ascenzi and Bonucci arrived to this conclusion by observing the osteons under polarized light (Ascenzi et al., 1973), which exhibits an alternate pattern, and the corresponding correlation with electron microscopy. In this work, a more recent approach to the sublamellar structure of an osteon will be considered in Section 3.

In addition, Ascenzi et al. (1973) referred that the fibrils of the innermost and outermost lamellae are essentially oriented in a circumferential direction. We note in passing that the cement line (1 μm thick) is not considered in the numerical models of this work because it is expected that this layer was fully damaged or eliminated during the osteon extraction process. In their work, these authors also consider another type of osteon (type 2), with lamellae showing a spiral course fibril arrangement, close to the axial direction of the osteon (see Fig. 3). Even in this type of osteon, Ascenzi and Bonucci reported that the fibrils of the innermost and outermost lamellae are essentially oriented in a circumferential direction.

Experimentally, and for type I osteons (the type analyzed in this work), it is verified that the application of a compressive radial load leads to the generation of microcracks in circumferential direction, as described in a comprehensive way by Ascenzi et al. (1973). These authors reported the following experimental evidences:

- Microcracks are circumferential and they appear mainly in the lamellae whose fibrils are aligned in the axial direction of the osteon (longitudinal lamellae). Some of them are located along the interfaces of the lamellae. In addition, microcracks extend through the whole thickness of the analyzed section.

- Microcracks begin in the longitudinal lamellae that are near the haversian canal.

- Microcracks appear in the four quadrants and concentrate in circular sectors located in a region between $20°$ and $50°$ with respect to the loading direction.

- The lamellae with fibrils essentially arranged in the circumferential direction (transverse lamellae) do not show apparent damage in this process.

Fig. 4 shows a portion of a tested osteon before the load application (left) and under the application of the load that causes the circumferential microcracks (right). Further analysis with electron microscopy shows that the microcracks within the longitudinal lamellae advance through the interfibrillar substance (that acts as a matrix), indicating that the strength of this substance is clearly lower than the fibril strength.

Recently, Ebacher et al. (2012) also carried out experimental tests by compressing a portion of cortical tissue in the radial direction. As will be commented in Section 7, their results are in full agreement with those observed by Ascenzi et al. (1973).

From all the above experimental observations, it can be inferred that the matrix failure that appears in the longitudinal lamellae is caused by either a normal tensile traction that acts in the radial direction, or a shear traction, or a combination of both. This behavior is analogous to the delamination processes that can be found in structural fiber-reinforced composite materials due to the existence of interlaminar stresses. Hence, in the numerical simulations of this work, we propose the application of failure criteria initially conceived for the delamination of composite laminates in order to explain the failure mechanisms of an osteon under this type of load.

3. ESTIMATION OF ELASTIC PROPERTIES OF LAMELLAE

There is a vast literature regarding the elastic properties of bone (Cowin, 2001), which have been mainly obtained through mechanical tests at the macroscopic level (Turner and Burr, 1993, e.g.). On the other hand, at the microscopic level, nanoindentation procedures (Zysset et al., 1999; Rho et al., 2002; Faingold et al., 2012) and ultrasound techniques (Rho et al., 1993; Katz et al., 1984), enable the characterization of local elastic constants for both cortical and trabecular bone tissues. In general, results show that the elastic behavior is clearly non-isotropic. There are also some approaches that estimate the elastic constants using hierarchical analytical models that consider the microstructure and the constituent properties (Cowin, 2001; Yoon and Cowin, 2008a,b; Reisinger et al., 2010; Martínez-Reina et al., 2011).

Currey (1962) and Bondfield and Li (1967) are among the first researchers that recognized a lamella as a two-phase composite, being the main constituent the mineralized collagen fibril, plus certain water content. Under this assumption, the collagen fibril can be regarded as a matrix in which the reinforcement crystals of hydroxyapatite (HA) are embedded. These crystals are arranged in a highly-orientated distribution, and hence the elastic behavior of the mineralized collagen fibrils can be considered approximately orthotropic. In the literature, different crystal shapes and dimensions are reported (Rubin et al., 2003, e.g.), which have allowed the development of micromechanical models based on analytical approaches. For example, Wagner and Weiner (1992) and Akiva et al. (1998) apply the Halpin-Tsai equations (often used in structural composites) to the estimation of the micromechanical elastic properties as a function of the hydroxyapatite crystal size.

Experimental evidence commented in previous Section 2 shows that the collagen fibril orientation plays an important role. There are many works in the literature that address the relevance of the orientation of the collagen fibrils at the lamellar level. Gebhardt (1906) observed that collagen fibrils change suddenly their orientation between adjacent lamellae. As did Ascenzi et al. (1973), a similar hypothesis was suggested by Weiner et al. (1991) and Wagner and Weiner (1992), differentiating between alternating thick and thin lamellae arranged concentrically around the haversian canal. In more recent works, each lamella is considered as a layered arrangement with a different fibril orientation pattern in each adjacent layer (Giraud-Guille, 1988; Akiva et al., 1998; Weiner et al., 1999; Wagermaier et al., 2006). Reisinger et al. (2011) have developed a detailed finite element analysis of a unit cell of the microstructure to estimate the elastic properties at the lamellar level. These authors analyze several orientation patterns and conclude that the model proposed by Weiner et al. (1999), based on a 5-layered structure in each individual lamella, is in good agreement with experimental results.

3.1. Elastic properties of the mineralized collagen fibril

In this work, we will follow the approach presented by the authors in Vercher et al. (2013). At the level of a single mineralized collagen fibril, a staggered arrangement of platelets is considered, according to the spatial distribution reported in the literature, e.g. by Rho et al. (1998); Orgel et al. (2001). A representative volume element (RVE) of a typical staggered structure of the mineralized fibril has been modelled using finite elements, see Fig. 5, imposing periodical boundary conditions. This enables the estimation of the constitutive elastic matrix of a collagen fibril by application of six independent unit-strain load cases.

The input parameters for the FE model of the fibril structure are taken from Reisinger et al. (2011). Collagen and HA mineral phases are assumed to be elastic isotropic with Young's modulus $E_{\mathrm{col}} = 5$ GPa (Cusak and Miller, 1979), $E_{\mathrm{ap}} = 110.5$ GPa (Yao et al., 2007), and Poisson's ratios $\nu_{\mathrm{col}} = 0.3$ and $\nu_{\mathrm{ap}} = 0.28$ (Yao et al., 2007). The resulting constitutive matrix for the homogenized behaviour of the mineralized fibril corresponds to a monoclinic material behavior, because there is only a single symmetry plane in the staggered crystal pattern. The platelet dimensions are $132 \times 30 \times 5$ nm, which are within the ranges reported by Rubin et al. (2003). The assumed volume fraction is $V_{\mathrm{f}} = 0.3$ and the RVE dimensions are $4.4d$ long (being d the periodic distance of 67 nm), 154 nm width and 32 nm thick (Vercher et al., 2013). Considering all these data, the 3D homogenized stiffness matrix of the mineralized collagen fibril $\mathbf{C}_{\mathrm{fib}}$ is:

$$\mathbf{C}_{\mathrm{fib}} = \begin{pmatrix} 31.790 & 7.008 & 4.115 & 0 & 1.066 & 0 \\ & 25.050 & 3.666 & 0 & 0.162 & 0 \\ & & 9.706 & 0 & 0.001 & 0 \\ & & & 2.789 & 0 & 0.219 \\ & \text{symm} & & & 2.888 & 0 \\ & & & & & 7.745 \end{pmatrix} \text{GPa} \qquad (1)$$

The volume fraction of 0.3 can be considered as a representative value of the total mineral content in both fibril and extrafibrillar matrix (Reisinger et al., 2011). For the above constitutive matrix, the cartesian reference system is the local system $(1, 2, 3)$ shown in Figs. 5 and 6. Therefore, the monoclinic symmetry plane is the 1-3 plane. The order of the components of the stress vector associated with (1) is $\boldsymbol{\sigma} = \{\sigma_{11}, \sigma_{22}, \sigma_{33}, \sigma_{23}, \sigma_{31}, \sigma_{12}\}^{\mathrm{T}}$ and analogously for the engineering strain vector $\boldsymbol{\varepsilon}$.

3.2. Elastic properties at the lamellar level

At this stage, we have considered the 5 sublamellae structure proposed by Weiner et al. (1999). The different mineralized fibril orientation pattern in each sublamellae is sketched in Fig. 7. In this work, these sublamellae have been condensed into two types of alternating lamellae: thin and thick lamellae. This simplified structure is in agreement with Weiner et al. (1991) and Wagner and Weiner (1992).

Currently, it is accepted that the fibril orientation pattern is an important feature because mechanical properties depend on bone structure at the very small scale (Reisinger et al., 2011). In this work, fibrils orientated circumferentially around the osteon are defined by the angle $\psi_1 = 0°$ and fibrils aligned with the osteon axis by the angle $\psi_1 = 90°$ (see angle definitions in Fig. 6). Starting from the thin lamella shown in Fig. 7, the orientation sequence of the five sublamellae is 0°, 30°, 60°, 90° and 120°, according to Weiner et al. (1999). There is an additional rotation ψ_2 around the fibril axis (axis 1) of the 4th and 5th sublayers, estimated as $\psi_2 = 70°$ and 30°, respectively (Vercher et al., 2013). The thickness T_i for each sublayer is assumed to be $T_i = (0.4, 0.2, 0.2, 1.8, 0.6)$ μm (Akiva et al., 1998). The grouping of the sublamellae into thin and thick lamellae yields the thicknesses $T_{\text{thin}} = 0.8$ μm for the thin lamellae and $T_{\text{thick}} = 2.4$ μm for the thick lamellae.

To obtain the equivalent elastic properties of each sublamellae, the Lekhnitskii transformation for non-isotropic constitutive matrices is applied. The stiffness matrix given in (1) in the local system $(1, 2, 3)$ is transformed according to the rotations ψ_1 and ψ_2 for each sublamellae into the local cartesian system (x, y, z) shown in Fig. 6, which is common for all sublamellae. Note that the directions (x, y, z) defined at each point are coincident with directions (θ, z, r), respectively, of the osteon cylindrical system.

Subsequently, the equivalent properties for thin and thick lamellae are obtained following a rule of mixtures approach. For each elastic property, denoted generically as D, the equivalent property is calculated as a weighted average proportional to the sublamellae thickness:

$$D_{\text{thin}} = \frac{1}{T_{\text{thin}}} \left(T_1 D_1 + T_2 D_2 + T_3 D_3 \right) \tag{2}$$

$$D_{\text{thick}} = \frac{1}{T_{\text{thick}}} \left(T_4 D_4 + T_5 D_5 \right) \tag{3}$$

As a result, the equivalent stiffness matrices of the thin and thick lamellae are:

$$\mathbf{C}_{\text{thin}} = \begin{pmatrix} 28.995 & 8.119 & 4.003 & -0.254 & 0.699 & 0.730 \\ & 25.625 & 3.779 & -0.166 & 0.335 & 0.730 \\ & & 9.706 & -0.0004 & 0.001 & 0.097 \\ & & & 2.814 & -0.021 & -0.014 \\ & \text{symm} & & & 2.863 & 0.124 \\ & & & & & 8.855 \end{pmatrix} \text{GPa} \tag{4}$$

$$\mathbf{C}_{\text{thick}} = \begin{pmatrix} 12.206 & 5.370 & 5.532 & -0.079 & -1.492 & -0.388 \\ & 30.572 & 6.369 & 0.251 & -1.065 & -0.304 \\ & & 18.804 & 0.270 & -3.682 & 0.363 \\ & & & 6.516 & -0.056 & 1.682 \\ & \text{symm} & & & 4.704 & -0.196 \\ & & & & & 4.684 \end{pmatrix} \text{GPa} \tag{5}$$

These matrices are expressed in the local system (x, y, z) of Fig. 6. The order of the components of the stress vector is $\boldsymbol{\sigma} = \{\sigma_{xx}, \sigma_{yy}, \sigma_{zz}, \sigma_{yz}, \sigma_{zx}, \sigma_{xy}\}^{\mathrm{T}}$. By identifying the local system (x, y, z) with the directions of the global cylindrical system of the osteon, the order of the components of the stress vector is $\boldsymbol{\sigma} = \{\sigma_{\theta\theta}, \sigma_{zz}, \sigma_{rr}, \sigma_{zr}, \sigma_{r\theta}, \sigma_{\theta z}\}^{\mathrm{T}}$ and analogously for the engineering strain vector $\boldsymbol{\varepsilon}$. It is important to point out that the linear elastic material behaviour considered in this work is valid under certain conditions of bone humidity and calcification (Ascenzi and Bonucci, 1967), as will be further commented in the following section.

4. ESTIMATION OF STRENGTH PROPERTIES OF LAMELLAE. FAILURE CRITERIA

Since the load condition analyzed in this work (compressive diametral loading, see Fig. 2) is essentially an in-plane loading state, it is expected that the failure is governed by the plane stress state shown in Fig. 7 in regions where circumferential (or hoop) $\sigma_{\theta\theta}$, radial σ_{rr} or shear $\sigma_{r\theta}$ stresses are high compared to their respective strength limits. Following customary terminology in structural composite materials, the circumferential stress $\sigma_{\theta\theta}$ can be considered an intralaminar stress, whereas σ_{rr}, $\sigma_{r\theta}$ correspond to interlaminar stresses that cause eventual delamination.

It is also expected that the thick lamellae exhibit a low strength to these stresses, because the mineralized collagen fibrils are essentially aligned in the out-of-plane direction (i.e. the osteon z-axis direction, see Fig. 7). For thick lamellae and for in-plane loads, the interfibrillar matrix is the main load-bearing material and its relative low strength can lead to matrix microcracking. This is in accordance with the experimental evidences commented in Section 2 and it is verified numerically in the following sections.

Ascenzi and Bonucci (1967, 1968, 1972) carried out extensive experimental testing on isolated osteons to characterize the tensile, compressive and shear properties of an osteon. In this work, we will estimate the strength properties from their tests on osteons subjected to tensile load in the osteon z-axis and from shear tests performed by application of a punch centered on the osteon in the z-axis. From all available data, we have considered the results for 25-30 year-old donors with a high calcification degree, determined by microradiography and tested on wet conditions. Osteons with a high calcification degree are stiffer, stronger and with a more linear elastic behaviour up to rupture than those with low calcification (Ascenzi and Bonucci, 1972).

It is well known that the stiffness and strength properties depend not only on the calcification degree, but also on the humidity condition and age (Ascenzi et al., 1973). The change in tensile stiffness and strength in the axial direction due to humidity is very significant, being larger for dry samples than for wet samples. The effect of the calcification degree is not so important although, as expected, it is shown that the stiffness and strength values are smaller for a low calcification degree. Finally, the influence of age is not so considerable.

Despite the fracture planes intersected some lacunae in their experimental tests, it is worth remarking that Ascenzi and Bonucci (1967, 1972) did not find a clear evidence that may correlate the lacunae density with the tensile or shear strengths. Note that cortical bone exhibits a considerable inelastic deformation, relaxing stress concentrations and increasing its toughness (Ebacher et al., 2012). It is often suggested that the strain amplification at the osteocyte lacunae increases the strain perceived by the osteocytes and the subsequent bone remodelling signaling (e.g. Prendergast and Huiskes, 1996; M.G. Ascenzi et al., 2013).

4.1. Circumferential tensile strength $S_{\theta\theta,t}$

Given the microfibril arrangement in the thin lamellae (see Fig. 7), the circumferential tensile strength of the thin lamellae must be clearly greater than for thick lamellae, i.e. $S^{\text{thin}}_{\theta\theta,\text{t}} > S^{\text{thick}}_{\theta\theta,\text{t}}$. As expected, Ascenzi and Bonucci reported that the maximum stiffness and strength for an osteon loaded in the axial z-axis is found for type II osteons (following the nomenclature of Fig. 3). With the exception of the innermost and outermost lamellae, type II osteons have lamellae oriented mainly in the axial direction of the osteon. The strength value of this type of osteons loaded in a tensile test was reported as 120 MPa in Ascenzi and Bonucci (1967) (for a dry condition, this value increases up to 193 MPa). Therefore, it seems reasonable to assume that the strength of a sublamella loaded in the fibril direction is about this value. Hence, the circumferential tensile strength of thin lamellae will be estimated as $S^{\text{thin}}_{\theta\theta,\text{t}} = 120$ MPa.

The estimation of the circumferential tensile strength for the thick lamellae is more elusive. From tensile tests carried out in the z-axis for type I osteons, Fig. 3, we have considered in this work that the onset of the failure of the weakest lamellae under the tensile test corresponds to a clear depart from the linear response in a σ-ε diagram. These diagrams are available in Ascenzi and Bonucci (1967) for type I osteons. Under a tensile test in z-axis for type I osteons, the first failure will occur for lamellae whose fibrils are orientated perpendicularly to the loading direction and this will introduce a loss of linear behaviour in the σ-ε response. This value has been estimated in an approximated way from Fig. 8, reproduced from Ascenzi and Bonucci (1967), and is about 50 MPa, that can be assumed to be the strength of a thin lamella when loaded in the osteon z-direction. We make a further assumption by considering that this strength is equal to the strength of a thick lamella when loaded in the circumferential direction and hence $S^{\text{thick}}_{\theta\theta,\text{t}} = 50$ MPa.

4.2. Radial tensile strength $S_{rr,t}$

A tensile failure in the radial direction is an interlaminar failure that implies the fracture of the interfibrillar matrix without affecting the mineralized collagen fibrils. Therefore, the radial tensile strength will be approximately the same for all sublamellae or their grouping into either thin or thick lamellae. Thus, we can write $S^{\text{thin}}_{rr,\text{t}} \approx S^{\text{thick}}_{rr,\text{t}}$ and it will simply denoted as $S_{rr,\text{t}}$.

Since this failure mode is similar to the failure mode of a thick lamella loaded circumferentially (both modes imply the damaging of the interfibrillar matrix), it is reasonable to assume that $S_{rr,\mathrm{t}} \approx S_{\theta\theta,\mathrm{t}}^{\mathrm{thick}} = 50$ MPa. When no better estimates are available, this hypothesis is also usual in the analysis of delamination of structural composite materials (Brewer and Lagacé, 1988).

4.3. Shear strength $S_{r\theta,s}$

Ascenzi and Bonucci (1972) carried out shear tests by micropunching the center of osteons in the axial direction. This type of test led to the separation, almost cylindrical, of a set of inner lamellae with respect the outer. Their results show that the shear stiffness and strength depend slightly on the type of osteon (I or II): the shear strength $S_{\mathrm{s,punch}}$ varies between 56 MPa for type I and 46 MPa for type II. It can be assumed that the shear strength of a thick lamella in the r-z plane (see reference system in Fig. 7) under the micropunch test is similar to the shear strength in the plane r-θ of a thin lamella. Therefore, we will assume that $S_{r\theta,\mathrm{s}}^{\mathrm{thin}} = 46$ MPa.

The shear strength in the plane r-θ for thick lamellae must be clearly lower than 46 MPa, since this shear mode does not involve the shearing of mineralized fibrils, which are essentially normal to the plane r-θ. The shearing failure will involve mainly shearing of the interfibrillar matrix. This value has been estimated as $S_{r\theta,\mathrm{s}}^{\mathrm{thick}} \approx 20$ MPa.

It is worth emphasizing that the estimated values given above must be considered as a first approximation, being the deviations large in practice due to several factors, such as calcification degree or water content. Another aspect not considered here is the variation of properties from inner lamellae to outer lamellae, which has been reported for elastic behaviour, e.g. in Faingold et al. (2012). The literature on strength properties is scarce and further research is necessary to have better characterization of the strength properties of these tissues.

4.4. Intralaminar and interlaminar failure criteria

Two independent failure criteria, intralaminar and interlaminar, will be considered for the in-plane analysis of an osteon under diametral compressive load. The intralaminar failure of a lamella requires the individual verification of the following relationship for each lamella:

$$\sigma_{\theta\theta}^{\mathrm{thin}} \geq S_{\theta\theta,\mathrm{t}}^{\mathrm{thin}} \tag{6a}$$

$$\sigma_{\theta\theta}^{\text{thick}} \geq S_{\theta\theta,\text{t}}^{\text{thick}}, \tag{6b}$$

which simply checks whether the lamella fails under circumferential tensile stress or not. Note that circumferential compressive stresses are considered not to lead to intralamellar failure. For the interlaminar failure, our proposal is to use the interactive quadratic criterion of Brewer and Lagacé (1988):

$$\left(\frac{\langle\sigma_{rr}\rangle}{S_{rr,\text{t}}}\right)^2 + \left(\frac{\sigma_{r\theta}}{S_{r\theta,\text{s}}}\right)^2 \geq 1 \tag{7}$$

The Macaulay bracket operator $\langle\ \rangle$ in the first term denotes the positive part and indicates that the radial stress must be included only if $\sigma_{rr} > 0$, because compressive radial stresses tend to close any eventual microcrack and therefore make no contribution to the interlaminar failure criterion. The criterion is interactive in the sense that accounts for the simultaneous contribution of the radial and shear stresses. In the context of structural composites, this criterion is used to predict delamination between laminate plies.

5. NUMERICAL MODEL

The aim of the proposed finite element model is to determine the in-plane stress distribution and predict the location of microcrack initiation and further propagation. The geometry has been simplified to a half circular ring, including 17 thin lamellae and thick lamellae, see Fig. 9. The alternating arrangement of these lamella resembles the type I osteon described by Ascenzi et al. (1973), see Fig. 3. The first lamella around the haversian canal is a thin lamella, with a dominant fibril orientation in the circumferential direction (Ascenzi et al., 1973). Although it is well known that lamellae have thickness variations, we have assumed that the thin and thick lamellae have a constant thickness of 0.8 μm and 2.4 μm, respectively, according to the grouping described in Section 3. The diameter of the haversian canal is 40 μm and hence the total diameter of the osteon is 148.8 μm. All these dimensions are in agreement with the secondary osteon dimensions reported in Cowin (2001). Due to the small thickness of the specimen tested by Ascenzi et al. (1973), sketched in Fig. 2, a plane stress condition has been assumed, with unit thickness. The applied pressure p is distributed along a 60° circular arc, being its magnitude increased through the analysis.

A structured mesh has been generated that facilitates the definition of the lamellae boundaries. Since some contact surface procedures are involved in the analysis, a 4-node bilinear element has been used (CPS4 in Abaqus). To ease the introduction of anisotropic properties and application of failure criteria, an essential feature of the model is the alignment of the material axes with the circumferential and radial directions of the osteon reference system, see Fig. 7. All the resulting stresses are also referred to the axes r and θ of Fig. 7.

The model also includes the presence of lacunae as ellipses, whose major and minor axis are 10 μm and 4 μm, respectively. The geometry of the lacunae is based on the features given by Prendergast and Huiskes (1996), where the lacunae are described as ellipsoids of dimensions 22μm $\times$ 9μm $\times$ 4μm, with a major axis forming about 26° with the osteon axis and located in the boundary between lamellae (Currey, 1962). Therefore, the ellipses modelled in this work are a section of the 3D ellipsoids, assuming all the intersected lacunae are located in the same transverse plane.

The spatial distribution of the lacunae is based on the data found in Cowin (2001), that report an average density in cortical bone of 460 lacunae per mm^2 and an average lacunae area of about 30 to 40 μm^2. From these data and the correlation with some images in the literature, we have included 10 lacunae in the half-model of an osteon shown in Fig. 9. A dedicated routine has been programmed to modify the structured mesh in order to include the lacunae. The routine eliminates the elements intersected by the lacunae and modifies the node location of the neighboring elements so as to match the lacuna boundary. Note that the material axes of the modified elements are also defined in accordance to the global circumferential and radial directions.

6. NUMERICAL PROCEDURES AND RESULTS

6.1. Failure initiation

In order to determine the interlaminar failure, the Brewer and Lagacé criterion (7) has been implemented in Abaqus and applied to the stress evolution resulting from increasing the applied pressure p. Fig. 10 shows a contour map of the value given by the left hand side of (7). The interlaminar failure initiates when this value is 1 and the first occurrence takes place in a thick lamella (indicated by an arrow), about 45° with respect the vertical axis and in the neighborhood of a lacuna that acts as a local stress raiser. The applied load at this instant is $p \approx 14$ MPa. The region where the failure initiates is in agreement with the experimental evidences commented in Section 2. The failure mode is mainly by interlaminar shear, since $\sigma_{r\theta}$ reaches its strength limit $S^{\text{thick}}_{r\theta,\text{s}} \approx 20$ MPa, as shown in Fig. 11(c). In Fig. 11(a) it can be observed that, in the regions of high $\sigma_{r\theta}$, the interlaminar radial stress σ_{rr} is small compared with its strength limit $S_{rr,\text{t}} = 50$ MPa, and therefore contributes very little to the failure criterion (7). The different shear limits in thick and thin lamellae and their interaction due to their different stiffnesses, tend to concentrate the failure initiation in regions at about 45° with the vertical axis. Note in Fig. 11(c) that the lacuna presence exacerbates the stress concentration locally, causing the failure initiation. However, this is not the fundamental cause of failure in these regions, which is ultimately due to the high level of shear stress.

The numerical model predicts the failure initiation in a thick lamella and near the boundary between the thick and the successive thin lamellae. Experimentally some microcracks are found inside the lamellae with fibrils aligned in the osteon direction (thick lamellae) and not necessarily at the boundary between lamellae. A plausible explanation of this discrepancy is that strength properties are not homogeneous inside each lamella, and that transitions in stiffness and strength between lamellae is not so abrupt as considered in our numerical model.

The intralaminar failure criterion given in (6) must also be checked. Fig. 11 (b) shows the contour plot for $\sigma_{\theta\theta}$ and it can be seen that the maximum hoop stress is reached at the innermost thin lamella and is slightly less than 60 MPa. Since the strength limit for this potential failure mode is $S^{\text{thin}}_{\theta\theta,\text{t}} = 120$ MPa, no failure is expected in this zone, as reported by Ascenzi et al. (1973). The hoop stress in the adjacent thick lamella is about 20 MPa, which is also less than the respective limit $S^{\text{thick}}_{\theta\theta,\text{t}} = 50$ MPa. Therefore, no failure is predicted by application of (6).

6.2. Interlaminar failure propagation using the node release technique

After determining the initiation of failure and its location, the propagation has been carried out using two different techniques: the node release technique and the progressive damage approach. In the node release technique (NRT), contact surfaces are defined along the prospective crack propagation direction. This technique is often used to model debonding of surfaces along a specified direction. It involves the definition of master and slave contact surfaces. This has been accomplished by duplication of nodes along the interfaces between thick and thin lamellae, where microcracks are expected to grow. The two surfaces are initially tied and act as a single surface until a prescribed failure or fracture criterion is satisfied. When the criterion is reached, the connection between the surfaces is released.

In combination with the contact procedures available in Abaqus, the same master and slave surfaces are used to enable the contact between crack faces after the microcrack growth. This contact exists due to the compressive nature of the applied load. The analysis of the proposed model is computationally expensive, especially because the number of potentially debonding and contacting surfaces is high (all interfaces between thick and thin lamellae). An implicit incremental approach has been used for the analysis of propagation, where debonding, contact and loss of stiffness is expected during the nonlinear analysis.

As explained, the initiation conditions at an interface are determined using the Brewer and Lagacé criterion (Fig. 10). Initially, only one node is released at this point. The eventual propagation of the microcrack (equivalent to a surface delamination) is also governed by the Brewer and Lagacé criterion. The Abaqus command `*Debond` is used to release the initially tied nodes as the load increases. In the simulation, initiation points of new microcracks depend on the previous microcrack evolution.

In order to evaluate the crack propagation condition, an approach based on energetic considerations, such as the strain energy release rate G should be considered. However, critical values for the specific energy at fracture G_c are not available at the interlamellar and intralamellar level. Hence, we resolved to use a stress-based approach considering the Brewer and Lagacé criterion at a certain characteristic distance d. The Abaqus command `*Debond` involves the values of contact pressure `CPRESS` and contact shear `CSHEAR`. The criterion is then evaluated at a distance d ahead the crack tips of the generated microcracks, thus avoiding the theoretical singularity at the crack tips. The problem turns out to be the choice of the distance d. We have chosen a distance $d = 1.5\ \mu$m ahead the crack tip, which provides reasonable results. A sensitivity analysis has been carried out regarding this distance, as commented at the end of this subsection.

In Fig. 12, the variation of `CSHEAR` for an interface surface is represented at three instants. The solid black lines represent the value of the shear stress along an interface between a thick and a thin lamella. The coloured blue-to-red lines are simply marker scales that quantify the value of the shear stress, from minimum (blue) to maximum (red) passeing through zero. The three subfigures represent different states of failure initiation and propagation.

The first plot Fig. 12(a) represents a continuous distribution of the interface shear before failure initiation (a surface without intersecting lacunae is represented for simplicity). Once the variable `CSHEAR` reaches a value close to the limit strength ± 20 MPa, a node is released at this point. Hence, the interface shear stress drops locally to 0, as shown in Fig. 12(b). Two incipient cracks along the interface have been formed (each with two crack tips), one on the left quadrant and the other one on the right quadrant. The shear stress drops to zero between the crack tips, because the crack faces are free from shear stresses (it has been assumed that there is no friction between crack faces). A further increase of the load causes the interface cracks to propagate, as in Fig. 12(c), where `CSHEAR` is 0 inside the cracks. Both cracks have grown along the interface surface. The region where the shear stress is zero has increased, i.e. the crack faces have become longer since both crack tips at each crack become apart during the crack growth.

Fig. 13 shows the contour maps for the Brewer and Lagacé where the red colour has 1.0 as an upper limit value. Values exceeding 1.0 are plotted in grey and represent the regions in which failure is initiated and propagated as the load is increased. From left to right and top to bottom, the plot (a) in Fig. 13 corresponds to the initiation location, in a state similar to the represented in Fig. 10, $p \approx 14.0$ MPa. Next plot (b) shows an advancing crack on the left quadrant and a new crack just initiated on the right quadrant when the load has been increased to $p \approx 16.6$ MPa. In successive plots, both cracks grow and other microcracks are initiated and eventually grow up to a generalized state of failure with several propagated microcracks. For the last plot (f), $p \approx 20.1$ MPa, the innermost thin lamella also starts failing due to high circumferential stresses. It has been verified that the intralaminar criterion (6) is not achieved at earlier stages. From Fig. 13, it can be observed that the numerical analysis here presented is in good agreement with the experimental behavior observed by Ascenzi et al. (1973).

Fig. 14 plots the applied pressure p versus the displacement of the load application point located on the vertical radius. The expected loss of stiffness under a compressive load is evidenced by the progressive reduction of the slope in the diagram. It can be observed that once the microdamage starts due essentially to the interlaminar shear stresses, the load bearing capacity of the system is notably reduced. Fig. 14 shows the results of a sensitivity analysis for three characteristic distances d, showing that qualitative differences are not large within a reasonable distance d compared to geometric dimensions.

6.3. Failure propagation using the progressive damage approach

The previous analysis using NRT leads to the propagation of explicit microcracks. Despite this is similar to the real behaviour shown in Fig. 4, this approach is computationally expensive and difficult to generalize to a representative volume with several osteons or to 3D models.

As an alternative, the failure propagation after initiation has also been simulated through a progressive damage approach. This approach is based on a nonlinear FE analysis in which the stiffness properties are reduced at the element level as the stress state reaches a failure condition (Tay et al., 2008). This approach has been successfully applied in structural composite materials, such as fiber reinforced laminates (e.g. Chang and Chang, 1987; Hou et al., 2000; Lapczyk and Hurtado, 2007; Tay et al., 2008). In the progressive damage approach, it is assumed that the material behavior is elastic-brittle, in the sense that there is no significative plastic deformation (Lapczyk and Hurtado, 2007). One important advantage is its relatively simple extension to 3D models, in contrast to the numerical modelling of explicit cracks using fracture mechanics, even using the extended finite element method XFEM. Obviously, the local solution in the vicinity of the damaged zone will not be as accurate as in a fracture mechanics approach, but the technique captures the global loss of stiffness and has proven to be very efficient for diffuse damage and for models with a large number of microcracks, provided the discretization is sufficiently refined.

The simplest approach to carry out the reduction of the elastic properties is the direct material property degradation, MPD (Chang and Chang, 1987; Hou et al., 2000; Tay et al., 2008). This method will be used in this work and consists in reducing the elastic properties by a fixed factor that can depend on the mode failure. Although its implementation is simple, it needs an *a priori* specification of the reduction factors. It is customary to assume that the stiffness in certain directions is reduced to 0 (Chang and Chang, 1987; Hou et al., 2000), although the analysis can lead to excessively conservative results and numerical difficulties. Tay et al. (2008) suggest that a constant reduction factor of 0.1 is common practice in the literature due to its simplicity and convergence advantages. Other approaches are based on continuum damage mechanics (CDM), with a less arbitrary formulation, often based on thermodynamic principles. In CDM, the damage variable can take a value in the continuous range $[0, 1]$, and therefore the softening introduced is not abrupt.

The MPD procedure used in this work to model the progressive damage of an osteon has been implemented in Abaqus and it is similar to the implementation of Chang and Chang (1987) for structural composites. Two field variables (`FV1` and `FV2`) have been defined by means of the user subroutine `USDFLD` (User Defined Field). The field variables are solution-dependent variables that enable the assignment of different material properties according to their values. Thus, `FV1`=0 and `FV2`=0 indicate no failure, `FV1`=1 and `FV2`=0 indicate interlaminar failure and `FV1`=0 and `FV2`=1 indicate intralaminar failure, see Table 1. For the no failure state the elastic moduli are not reduced and for the failed state all the elastic moduli are reduced to 5% of their original values.

The field variables are solution-dependent variables in the sense that they are functions of the FE solution at the integration points (in our case, function of the stresses). In the user subroutine `USDFLD`, the failure criteria (6) and (7) are evaluated at each increment considering the strength limits defined in Section 4 as input parameters. The values on the left hand side of the criteria are stored at each increment as state variables (`STATEV` in Abaqus). On the other hand, the field variables `FV` are initialized to 0 when the analysis starts and only when any state variable `STATEV` is equal or greater than 1.0, the corresponding field variable `FV` is changed to 1 (damaged state). The field variable `FV` will remain as 1, even when the local stresses are reduced significantly, indicating the irreversibility of the damage process.

Fig. 15 shows the sequence of damaged elements according to the Brewer and Lagacé criterion (7). As explained above, the damage initiation is governed by interlaminar shear stresses in a thick lamella at about $p \approx 14$ MPa. The damage is mainly located near the stress concentration region next to a lacuna on the left quadrant. When the load is increased to $p \approx 20.1$ MPa, propagation of damage follows the elements in thick lamellae in a very similar pattern to the one predicted with the NRT, Fig. 13.

The progressive damage approach easily allows for computing advanced states of damage. Fig. 16 shows a generalized state of damage for applied pressures that are higher than the loads considered in Figs. 13 and 15. It can be observed that damage due to interlaminar stresses tends to concentrate in the thick lamellae. It is worth noting that damaged zones approximately match the observed experimental regions, located at about 20° and 50° with respect the vertical radius. Eventually, for the highest load, damage is generalized and extends also across thin lamellae.

As far as the intralaminar criterion (6) is concerned, damaged elements are shown in Fig. 17. Tensile circumferential stresses cause damage in the innermost lamellae, being the first a thin lamellae. The load for the initiation of this damage is relatively high (about 24 MPa), and therefore this type of damage is expected to occur only when the interlaminar failure shown in Fig. 15 is well developed. As a consequence, we can conclude that interlaminar shear stresses are the main cause of failure for this type of osteon under compressive diametral load, causing a separation of thin and thick lamellae.

7. DISCUSSION

In the previous analyses using either NRT or a progressive damage approach, the global effect of the microdamage process is the loss of stiffness of the system. In order to show this behaviour, Fig. 18 plots the applied pressure p versus the displacement of the load application point located on the vertical radius for both analyses.

Both procedures tend to yield similar behaviour curves in a global sense, although some differences can be appreciated just after damage initiation (about $p = 14$ MPa) due to the different approach used to introduce the defects: interface microcracks versus whole element damage. The reason of this difference is that the loss of stiffness under compressive load with the microcrack approach (NRT) is only in the circumferential direction but not in the radial direction, because crack face contact is allowed during the analysis. On the other hand, the reduction of the elastic properties in the progressive damage approach is applied to all elastic moduli equally, experiencing a loss of stiffness in all directions. In this sense, we can say that the NRT is more accurate than the progressive damage approach, but computationally much more expensive (NRT computation time is about eight times greater than with progressive damage). Other important disadvantages of the NRT approach are the difficulties for preprocessing (generation of contact surfaces) and the intrinsic difficulties for extending the procedure to 3D models or larger models that contain a representative volume of bone tissue. Given the similar global response shown in Fig. 18, we consider that the progressive damage approach can be an appealing approach to address this type of analysis.

The models and procedures here presented reproduce the trend observed experimentally by Ascenzi et al. (1973). This is confirmed by other recent experimental evidences reported by Ebacher et al. (2012). These authors examined the microcracks that appear at the lamellar and sublamellar levels in human cortical bone samples under compressive tests, see Fig. 19 (a) and (b). Their samples were analyzed by laser scanning confocal microscopy (LSCM) and reveal the great importance of the lamellar microstructure for the damage pattern observed. The damage pattern exhibits an alternate presence of circumferential microcracks that is related to the lamellar structure, thus confirming the behaviour observed by Ascenzi et al. (1973) and the predictions performed by our numerical models. This pattern is in line with the observations of Ebacher and Wang (2009), by which the stable development of multiple lamellar microcracks redistributes the stress around each haversian canal.

In their studies, Ebacher et al. (2012) state that all cracks start at lower hierarchical levels of bone and that the observed high density of microcracks improves the inelastic strain capacity of the lamellae. The role of canaliculi, widely spread over the lamellar tissue, in the microdamage initiation is also emphasized. Therefore, a smeared damage approach to model microcracks, such as the one proposed here, seems to be a convenient way to numerically simulate the real behaviour.

8. CONCLUSIONS

Two numerical approaches have been proposed for the analysis of failure at the lamellar level in osteons. The first is based on modelling explicitly interface microcracks and predicting their propagation using the so-called node release technique. The second approach follows a progressive degradation of elastic properties at the element level to simulate the loss of stiffness of damaged elements. The procedures have been applied to the mechanical behaviour of tests of an osteon under compressive diametral load, for which damage patterns are available in the literature. The elastic properties at the lamellar level have been estimated considering the equivalent elastic properties of a mineralized collagen fibril and the 5-sublamellar structure described in Weiner et al. (1999), whereas the strength properties have been inferred from different mechanical tests performed by Ascenzi and Bonucci on single osteons. In addition, intralaminar and interlaminar failure criteria have been implemented to ascertain the failure initiation and propagation under both mode failures.

From the numerical analyses, the dominant failure mode under compressive diametral load can be attributed to interlaminar shear stresses that affect the thin and thick lamellae in a different way. As a result, microcracks and damage initiate and spread circumferentially along lamellae whose reinforcement is essentially aligned with the osteon axis. The obtained damage patterns correlate well with the experimental images obtained by (Ascenzi et al., 1973; Ebacher et al., 2012), as regards its alternate character and the angular and radial location.

Both methodologies show promising strategies for further microdamage models of cortical tissue and its analysis under a mechanistic approach, especially the progressive damage approach for its reduced computational cost. This reduced computational cost becomes crucial when dealing with more complicated models, such as 3D models that include several osteons, interstitial matrix, different loading conditions, etc. Given that micromechanical strength properties are generally elusive to determine, numerical models of this kind can be of interest to simulate experimental tests and hence estimate strength properties using inverse identification procedures.

ACKNOWLEDGEMENTS

The authors wish to thank the Ministerio de Economía y Competitividad for the support received in the framework of the projects DPI2010-20990 and DPI2013-46641-R and to the Generalitat Valenciana, Programme PROMETEO 2012/023. The authors also thank Mr. Carlos Pons Gómez for his help in the development of some of the numerical models.

References

ABAQUS/Standard User's Manual, v. 6.12, Simulia, Providence, Rhode Island, 2012.

Akiva, U., Wagner, H.D., Weiner, S., 1998. Modelling the three-dimensional elastic constants of parallel-fibred and lamellar bone. Journal of Materials Science 33, 1497–1509.

Ascenzi, A., Bonucci, E., 1967. The tensile properties of single osteons. Anatomical Record 158, 375–386.

Ascenzi, A., Bonucci, E., 1968. The compressive properties of single osteons. Anatomical Record 161, 377–392.

Ascenzi, A., Bonucci, E., 1972. The shearing properties of single osteons. Anatomical Record 172, 499–510.

Ascenzi, A., Bonucci, E., Simkin, A., 1973. An approach to the mechanical properties of single osteonic lamellae. Journal of Biomechanics 6, 227–235.

Ascenzi, M.G., Lomovtsev A., 2006. Collagen orientation patterns in human secondary osteons, quantified in the radial direction by confocal microscopy. Journal of Structural Biology 153, 14-30.

Ascenzi, M.G., Kawas, N.P., Lutz, A., Kardas, D., Nackenhorst, U., Keyak, J.H., 2013. Individual-specific multi-scale finite element simulation of cortical bone of human proximal femur. Journal of Computational Physics 244, 298-311.

Bondfield, W., Li, C.H., 1967. Anisotropy of nonelastic flow in bone. Journal of Applied Physics 38, 2450–2455.

Brewer, A., Lagacé, P.A., 1988. Quadratic stress criterion for initiation of delamination. Journal of Composite Materials 22, 1141–1155.

Chang, F.K., Chang, K.Y., 1987. A progressive damage model for laminated composites containing stress concentrations. Journal of Composite Materials 21, 834–855.

Cowin, S.C., ed. Bone Mechanics Handbook. CRC Press. Boca Ratón, Florida, 2001.

Currey, J.D., 1962. Strength of bone. Nature 195, 513–514.

Cusack, S., Miller, A., 1979. Determination of the elastic constants of collagen by brillouin light scattering. Journal of Molecular Biology 135, 39–51.

Ebacher, V., Wang, R., 2009. A unique microcracking process associated with the inelastic deformation of Haversian bone. Advanced Functional Materials 19, 57–66.

Ebacher, V., Guy, P., Oxland, T.R., Wang, R., 2012. Sub-lamellar microcracking and roles of canaliculi in human cortical bone. Acta Biomaterialia 8, 1093–1100.

Faingold, A., Sidney, R.C., Wagner, H.D., 2012. Nanoindentation of osteonal bone lamellae. Journal of the Mechanical Behavior of Biomedical Materials 9, 198–206

Gebhardt, W., 1906. Über funktionell wichtige Anordnungsweisen der feineren und größeren Bauelemente des Wirbeltierknochens. Wilhelm Roux' Archiv für Entwicklungsmechanik der Organismen 20, 187–322.

Giraud-Guille, M., 1988. Twisted plywood architecture of collagen fibrils in human compact bone osteons. Calcified Tissue International 42, 167–180.

Hou, J.P., Petrinic, N., Ruiz, C., Hallett, S.R., 2000. Prediction of impact damage in composite plates. Composites Science and Technology 60, 273–281.

Katz, J.L., Yoon, H.S., Lipson, S., Maharidge, R., Meunier, A., Christel, P., 1984. The effects of remodeling on the elastic properties of bone. Calcified Tissue International 36, s31–s36.

Lapczyk, I., Hurtado, J.A., 2007. Progressive damage modeling in fiber-reinforced materials. Composites Part A: Applied Science and Manufacturing 38, 2333–2341.

Martínez-Reina, J., García-Aznar, J.M., Domínguez, J., Doblaré, M., 2009. A bone remodelling model including the directional activity of BMUs. Biomechanics and Modeling in Mechanobiology 8, 111–127.

Martínez-Reina, J., Domínguez, J., García-Aznar, J.M., 2011. Effect of porosity and mineral content on the elastic constants of cortical bone: a multiscale approach. Biomechanics and Modeling in Mechanobiology 10, 309–322.

Nalla, R.K., Kinney, J.H., Ritchie, R.O., 2003. Mechanistic fracture criteria for the failure of human cortical bone. Nature Materials 2, 164–168.

Orgel, J.P.R.O., Miller, A., Irving, T.C., Fischetti, R.F., Hammersley, A.P., Wess, T.J., 2001. The in situ supermolecular structure of type I collagen. Structure 9, 1061-1069.

Prendergast, P.J., Huiskes, R., 1996. Microdamage and osteocyte-lacuna strain in bone: a microstructural finite element analysis. Journal of Biomechanical Engineering, Transactions of the ASME 118, 240–246.

Reisinger, A.G., Pahr, D.H., Zysset, P.K., 2010. Sensitivity analysis and parametric study of elastic properties of an unidirectional mineralized bone fibril-array using mean field methods. Biomechanics and Modeling in Mechanobiology 9, 499–510.

Reisinger, A.G., Pahr, D.H., Zysset, P.K., 2011. Elastic anisotropy of bone lamellae as a function of fibril orientation pattern. Biomechanics and Modeling in Mechanobiology 10, 67–77.

Rho, J.Y., Ashman, R.B., Turner, C.H., 1993. Young's modulus of trabecular and cortical bone material: ultrasonic and microtensile measurements. Journal of Biomechanics 26, 111–119.

Rho, J.Y., Kuhn-Spearing, L., Zioupos, P., 1998. Mechanical properties and the hierarchical structure of bone. Medical Engineering & Physics 20, 92-102.

Rho, J.Y., Zioupos, P., Currey, J.D., Pharr, G.M., 2002. Microstructural elasticity and regional heterogeneity in human femoral bone of various ages examined by nano-indentation. Journal of Biomechanics 35, 189–198.

Ritchie, R.O., Kinney, J.H., Kruzic, J.J., Nalla, R.K., 2005. A fracture mechanics and mechanistic approach to the failure of cortical bone. Fatigue and Fracture of Engineering Materials and Structures 28, 345–371.

Rubin, M.A., Jasiuk, I., Taylor, J., Rubin, J., Ganey, T., Apkarian, R.P., 2003. TEM analysis of the nanostructure of normal and osteoporotic human trabecular bone. Bone 33, 270–282.

Tay, T.E., Liu, G., Tan, V.B.C., Sun, X.S., Pham, D.C., 2008. Progressive failure analysis of composites. Journal of Composite Materials 42, 1921–1966.

Taylor, D., 2007. Fracture and repair of bone: a multiscale problem. Journal of Materials Science 42, 8911–8918.

Taylor, D., Hazenberg, J.G., Lee, T.C., 2007. Living with cracks: Damage and repair in human bone. Nature Materials 6, 263–268.

Turner, C.H., Burr, D.B., 1993. Basic biomechanical measurements of bone: a tutorial. Bone 14, 595–608.

Vashishth, D., 2007. Hierarchy of bone microdamage at multiple length scales. Int J Fatigue 29, 1024–1033.

Vercher, A., Giner, E., Arango, C., Tarancón, J.E., Fuenmayor, F.J., 2014. Homogenized stiffness matrices for mineralized collagen fibrils and lamellar bone using unit cell finite element models. Biomechanics and Modeling in Mechanobiology 13, 437–449.

Wagermaier, W., Gupta, H.S., Gourrier, A., Burghammer, M., Roschger, P., Fratzl, P., 2006. Spiral twisting of fiber orientation inside bone lamellae. Biointerphases 1, 1–5.

Wagner, H.D., Weiner, S., 1992. On the relationship between the microstructure of bone and its mechanical stiffness. Journal of Biomechanics 25, 1311–1320.

Weiner, S., Arad, T., Traub, W., 1991. Crystal organization in rat bone lamellae. FEBS Letters 285, 49–54.

Weiner, S., Traub, W., Wagner, H., 1999. Lamellar bone: structure-function relations. Journal of Structural Biology 126, 241–255.

Yang, Q.D., Cox, B.N., Nalla, R.K., Ritchie, R.O., 2006. Fracture length scales in human cortical bone: the necessity of nonlinear fracture models. Biomaterials 27, 2095–2113.

Yao, H., Ouyang, L., Ching, W., 2007. *Ab initio* calculation of elastic constants of ceramic crystals. Journal of the American Ceramic Society 90, 3194–3204.

Yoon, Y.J., Cowin, S.C., 2008. The estimated elastic constants for a single bone osteonal lamella. Biomechanics and Modeling in Mechanobiology 7, 1-11.

Yoon, Y.J., Cowin, S.C., 2008. An estimate of anisotropic poroelastic constants of an osteon. Biomechanics and Modeling in Mechanobiology 7, 13-26.

Zysset, P.K., Guo, X.D., Hoffler, C.E., Moore, K.E., Goldstein, S.A., 1999. Elastic modulus and hardness of cortical and trabecular bone lamellae measured by nanoindentation in the human femur. Journal of Biomechanics 32, 1005–1012.

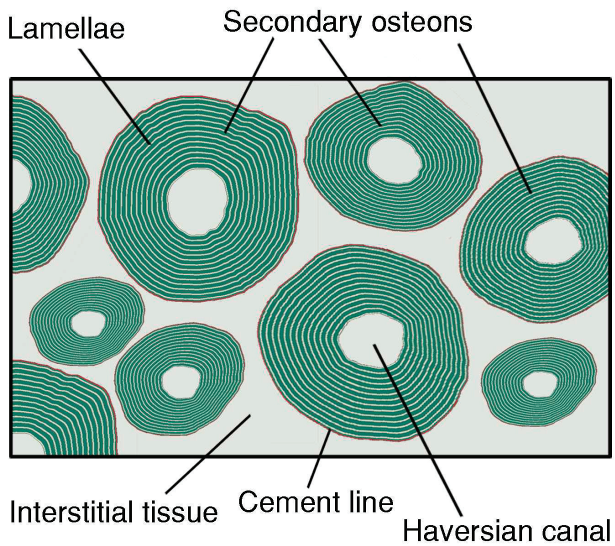

Figure 1: Schematic representation of the main morphological features of the cortical bone tissue at the microstructural level.

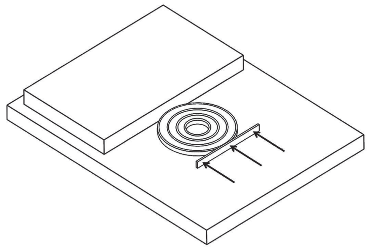

Figure 2: Radial compressive loading test (Ascenzi et al., 1973)

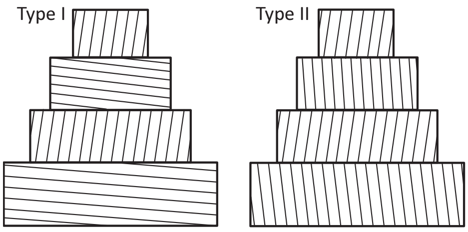

Figure 3: Sketch of the laminated structure of osteon types I and II, following Ascenzi et al. (1973).

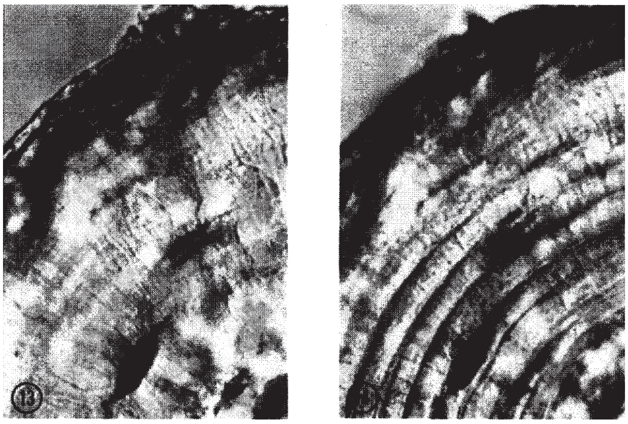

Figure 4: Behavior under compressive load of an osteon type I: left, before the loading; right, after the loading, showing the generation of microcracks. Reprinted from Ascenzi et al. (1973) with permission of Elsevier.

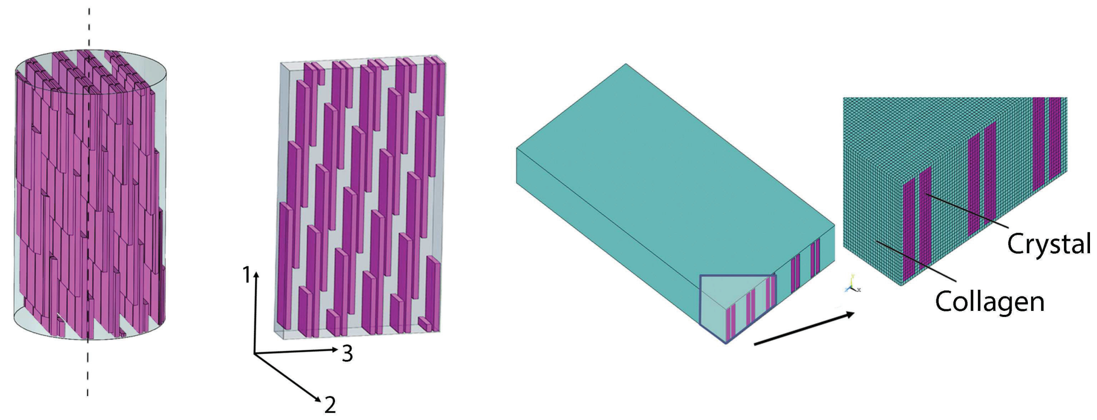

Figure 5: Representative volume element of a typical fibril structure modelled using finite elements by imposing periodical boundary conditions. The local coordinate system $(1, 2, 3)$ is associated with the fibril orientation.

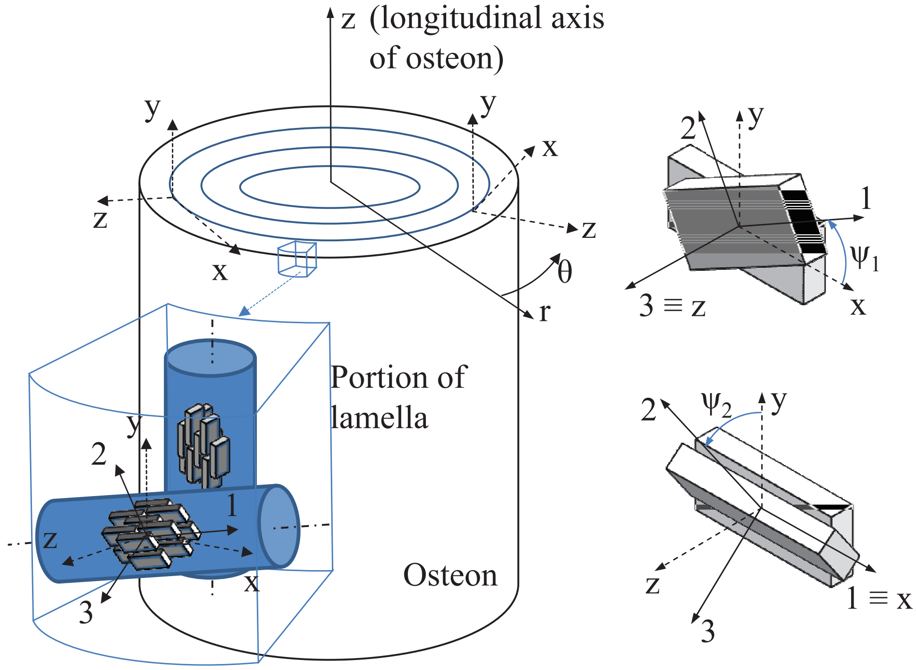

Figure 6: Coordinate system scheme. The local coordinate system $(1, 2, 3)$ is aligned with each mineralized fibril. The cylindrical coordinate system (r, θ, z) is used as a global coordinate system and a local auxiliary coordinate system (x, y, z) is defined at any point, being (x, y, z) coincident with (θ, z, r) respectively. Definition of angles ψ_1 and ψ_2 that determine the crystal orientation.

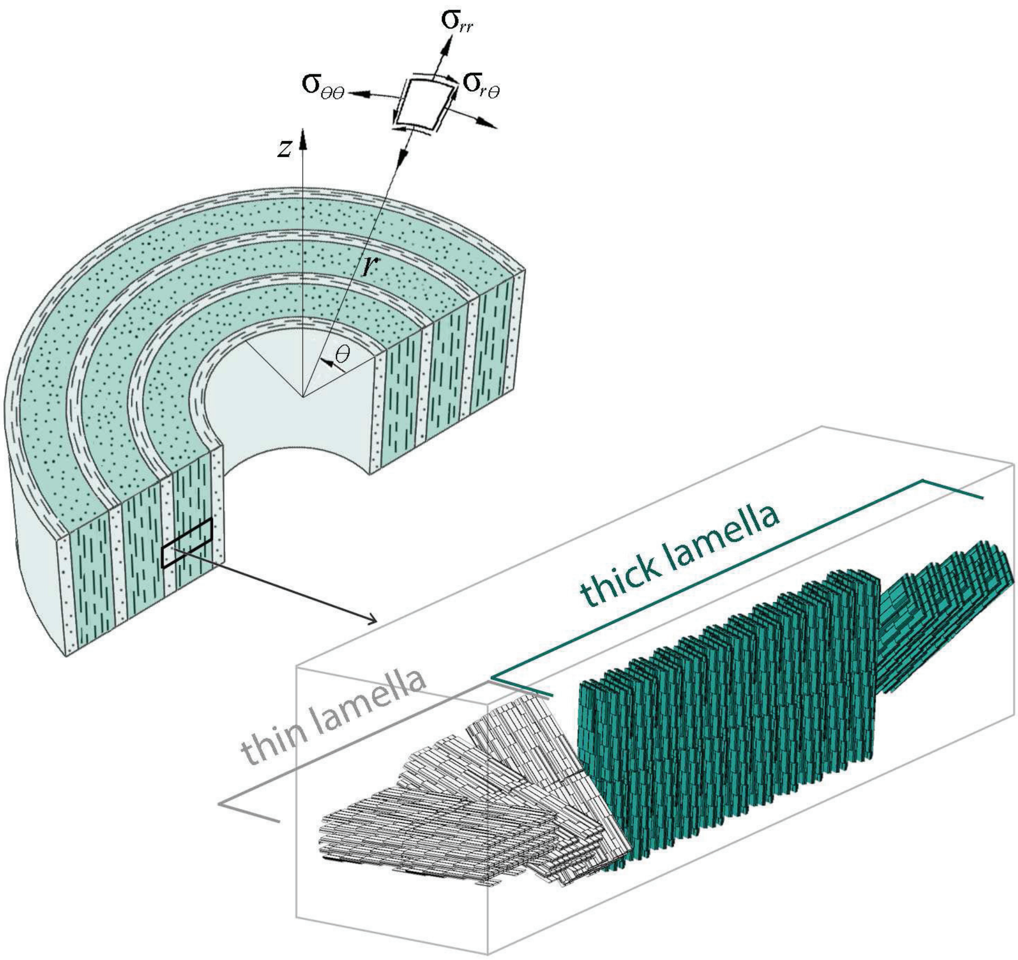

Figure 7: Model of an osteon with thin and thick lamellae, showing the cylindrical reference system (r, θ, z) aligned with the osteon axis. Condensation of the 5 sublamellar structure, with different mineralized fibril orientations, into two equivalent layers: thin and thick lamellae.

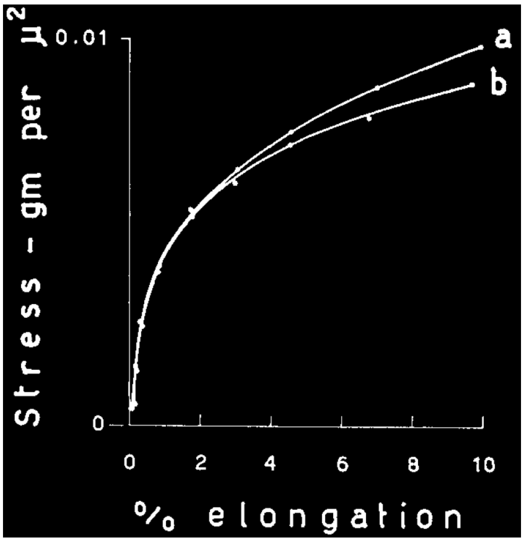

Figure 8: Stress-strain curves for tensile tests in the z-axis of single osteons. Curve (a) corresponds to a wet and fully calcified type I osteon, taken from a man of 30. Curve (b) Same from a man of 80. Note: 1 gr/μm^2 $\approx 10^4$ MPa. Reprinted from Ascenzi and Bonucci (1967) with permission of John Wiley and Sons.

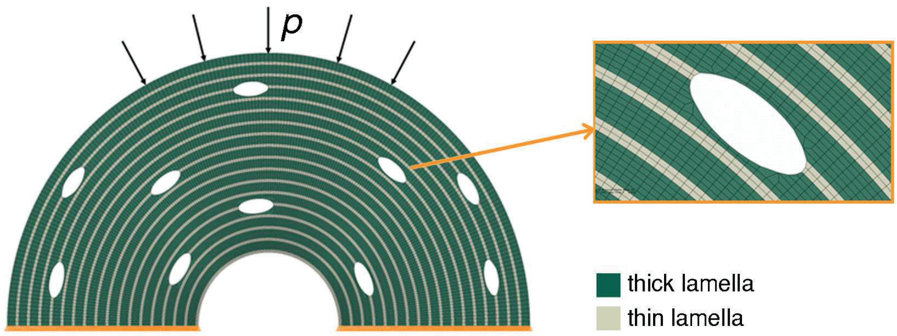

Figure 9: Finite element model, showing the applied load, the displacement constraints, the lamellae and the lacunae considered. The mesh is structured, enabling the arrangement into thin and thick lamellae of constant thickness and the cylindrical orientation of the material axis for each lamella. The detailed view shows the modification of the structured mesh to allow for the presence of lacunae.

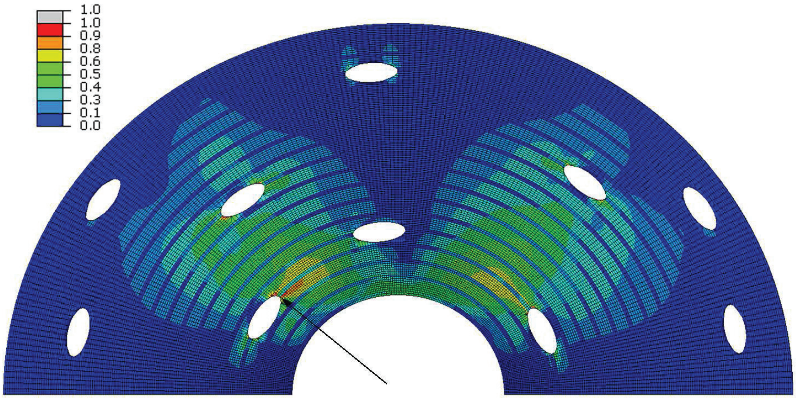

Figure 10: Initiation criterion. Application of the failure criterion of Brewer and Lagacé to determine the initiation of failure, reached at a load of $p \approx 14$ MPa.

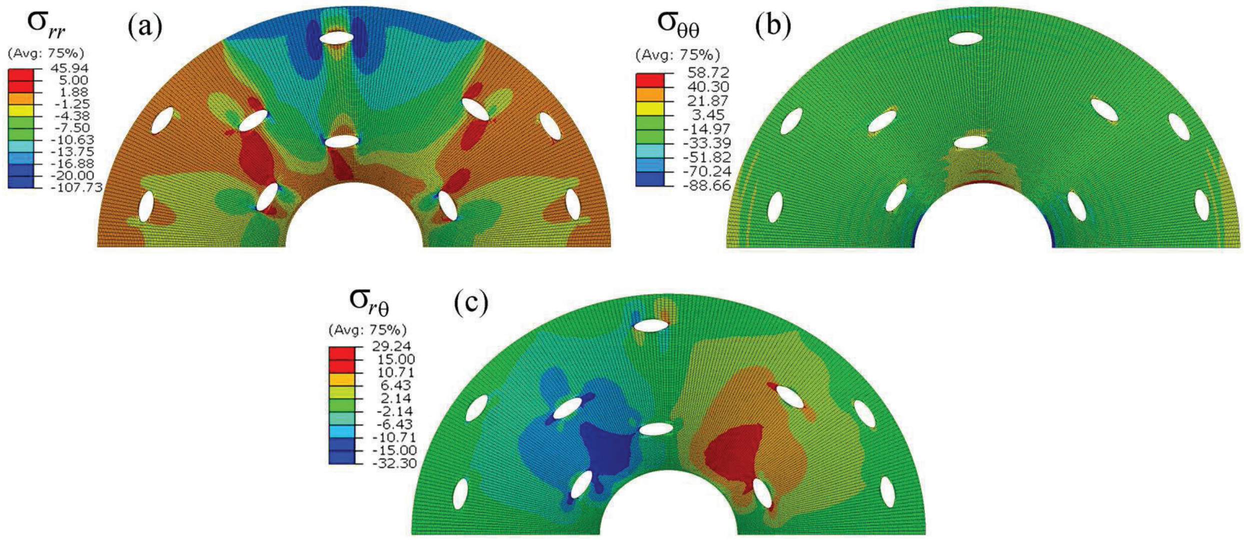

Figure 11: Stress fields (a) σ_{rr}, (b) $\sigma_{\theta\theta}$ and (c) $\sigma_{r\theta}$ for the failure initiation load of $p \approx 14$ MPa, shown in Fig. 10.

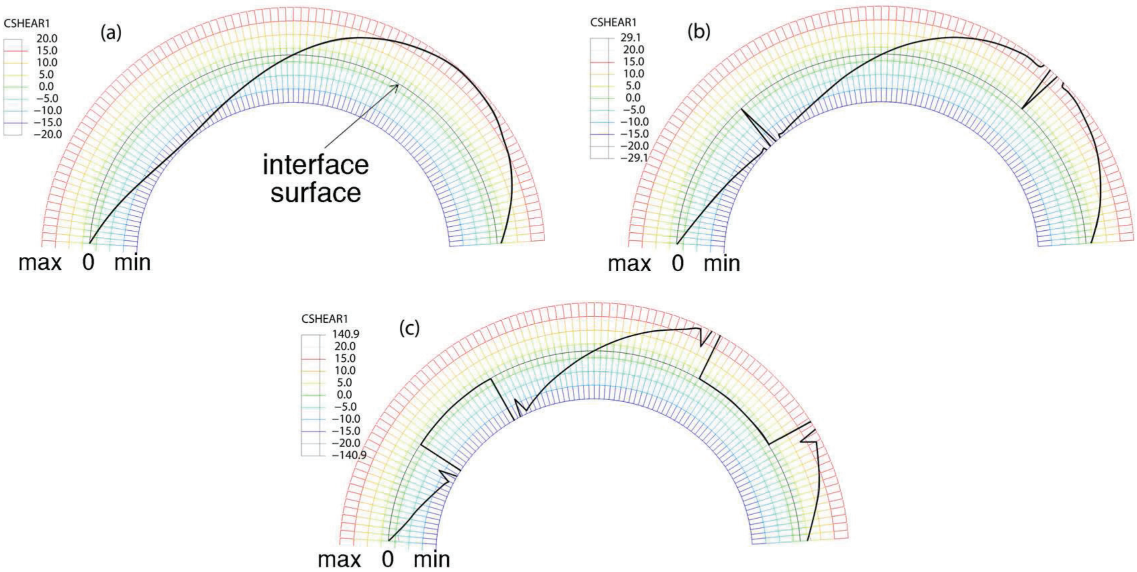

Figure 12: Node release technique. Evolution of shear stress along one of the contact surfaces (CSHEAR in Abaqus). For the sake of clarity, the surface does not intersect any lacunae. (a) Stress state before microcrack initiation; (b) microcrack initiation; (c) microcrack propagation.

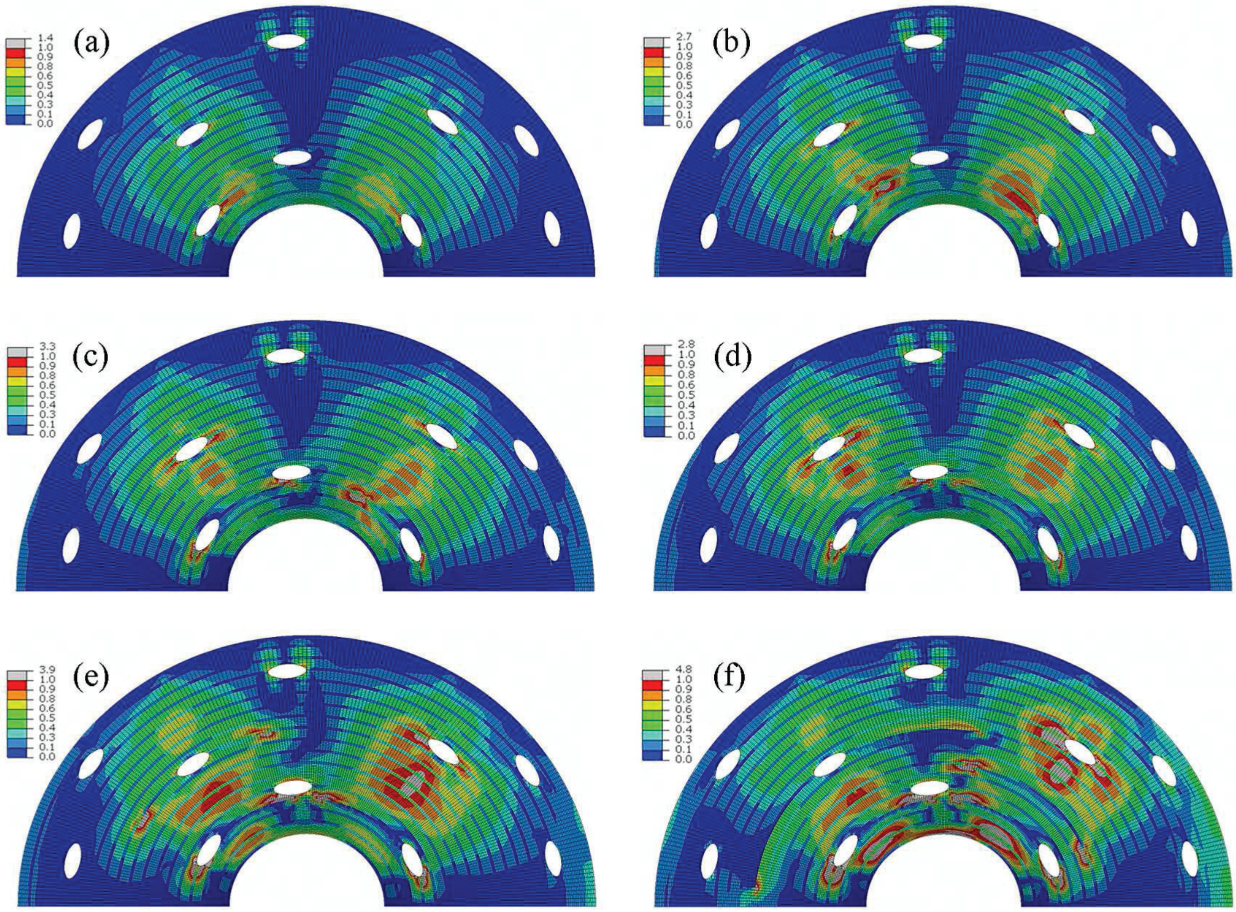

Figure 13: Node release technique. Evolution of the Brewer and Lagacé criterion for six instants of the microcracks initiation and propagation sequence. The instants correspond to the following applied pressures: (a) $p \approx 14.0$ MPa, (b) $p \approx 16.6$ MPa, (c) $p \approx 18.0$ MPa, (d) $p \approx 18.1$ MPa, (e) $p \approx 19.1$ MPa, (f) $p \approx 20.1$ MPa.

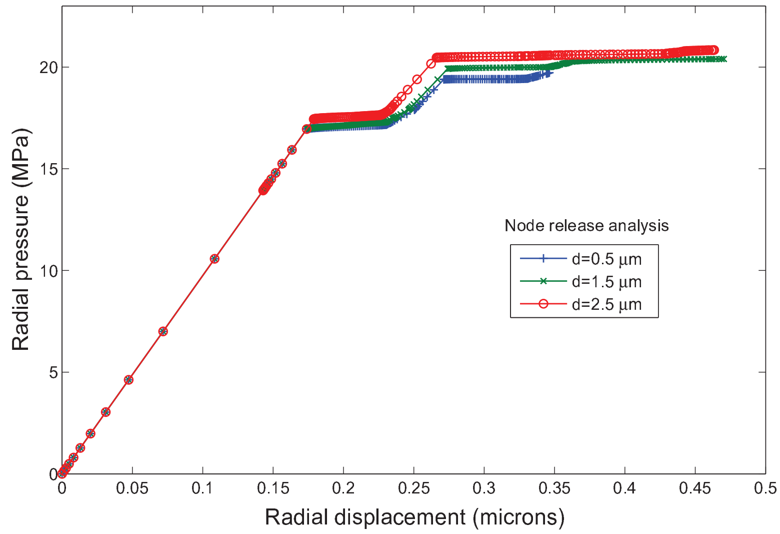

Figure 14: Node release technique. Sensitivity analysis to the characteristic length d used in the application of the procedure.

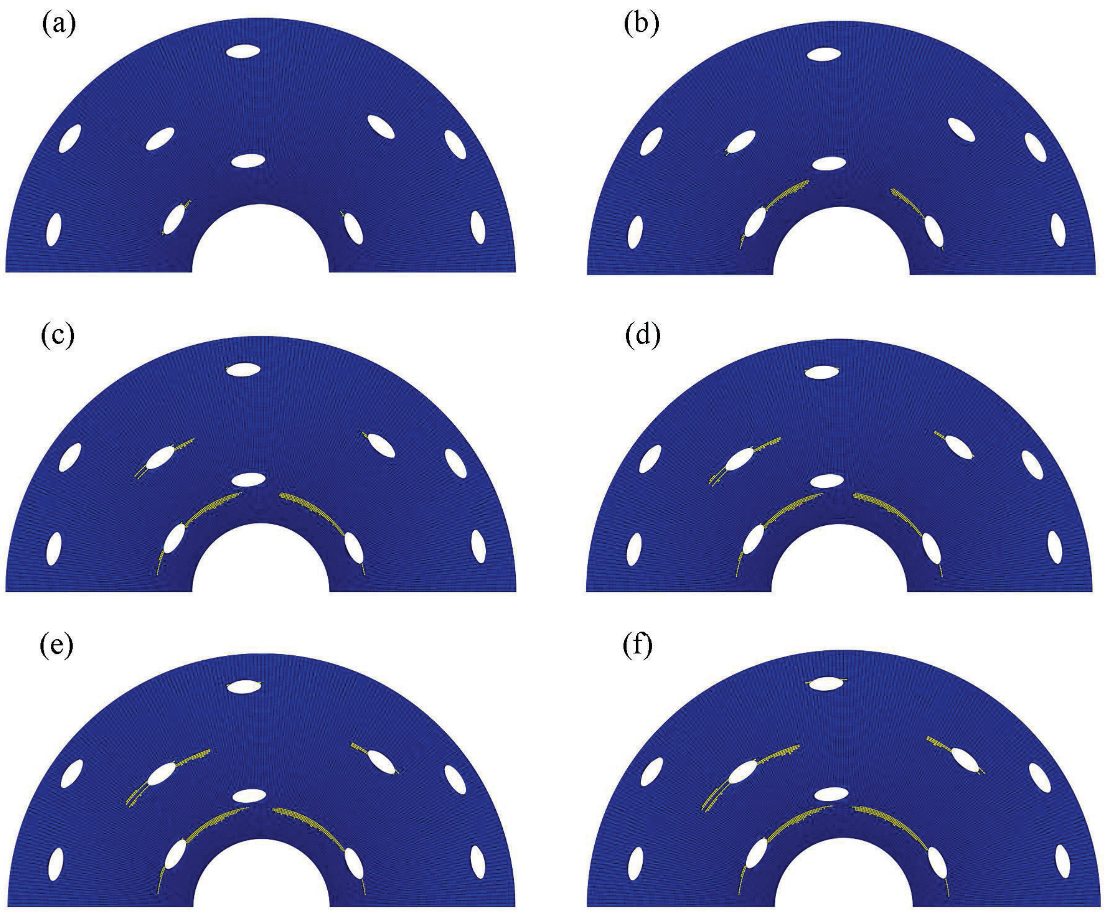

Figure 15: Progressive damage approach. Evolution of damaged elements (shown in yellow) by application of the interlaminar failure criterion of Brewer and Lagacé (7) for six instants of the damage propagation sequence. The instants correspond to the following applied pressures: (a) $p \approx 14.0$ MPa, (b) $p \approx 16.6$ MPa, (c) $p \approx 18.0$ MPa, (d) $p \approx 18.1$ MPa, (e) $p \approx 19.1$ MPa, (f) $p \approx 20.1$ MPa.

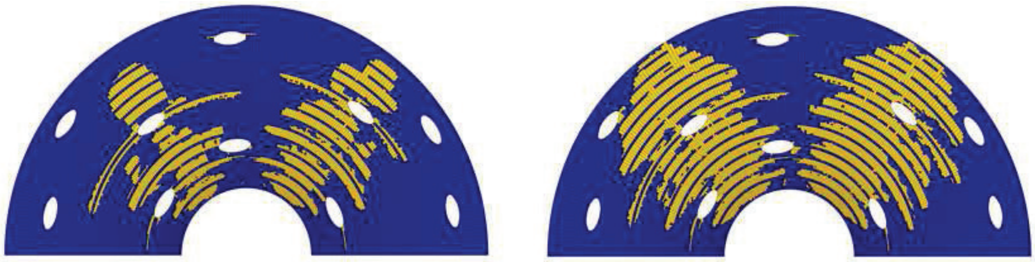

Figure 16: Progressive damage approach. Damaged elements (shown in yellow) by application of the interlaminar failure criterion of Brewer and Lagacé (7) for two advanced loading states (left, $p \approx 29.3$ MPa; right, $p \approx 31.5$ MPa.

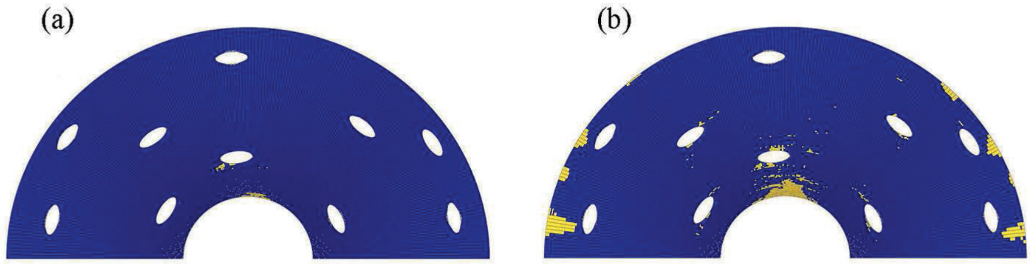

Figure 17: Progressive damage approach. Evolution of damaged elements (shown in yellow) by application of the intralaminar failure criterion (6) for two instants of the damage propagation sequence.

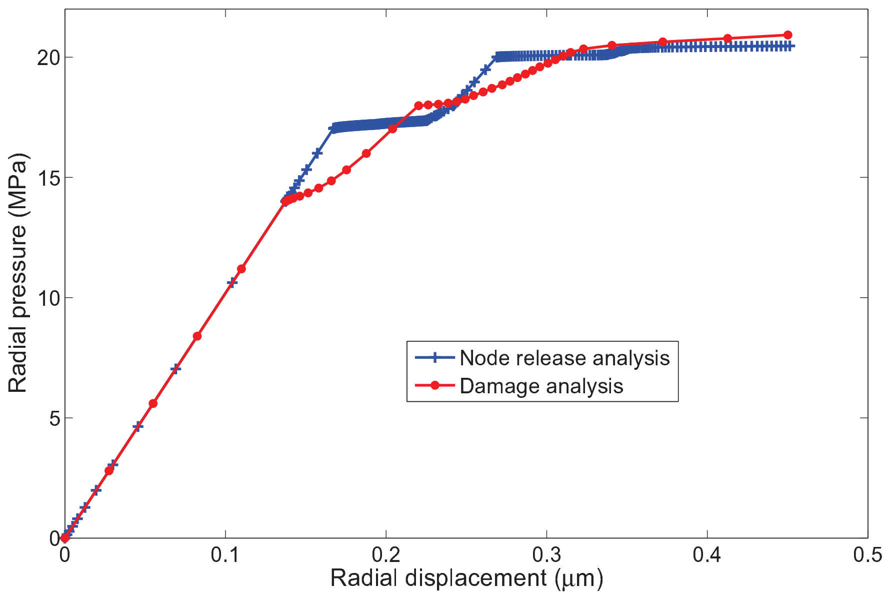

Figure 18: Comparative evolution of the applied pressure vs. the displacement of the load application point located on the vertical radius. Results for both techniques: node release technique and progressive damage approach.

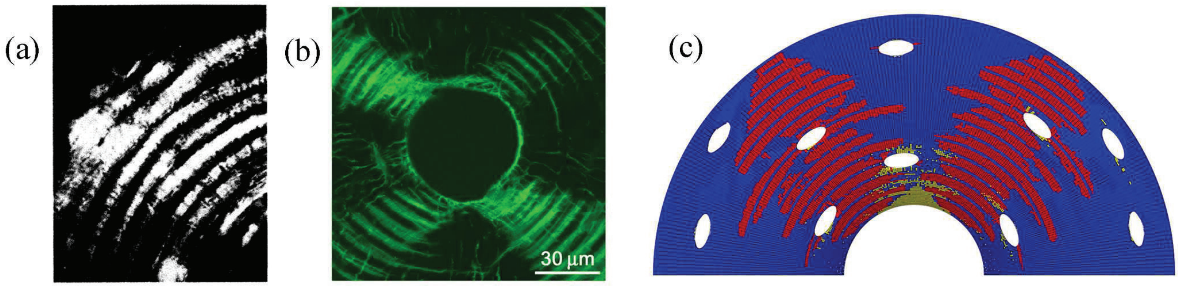

Figure 19: (a) and (b) Experimental images showing the damage in an osteon resulting from a radial compressive load, reported in Ascenzi et al. (1973) and Ebacher et al. (2012), both reprinted with permission of Elsevier. (c) Fields of progressive damaged elements for an advanced load state. In red, damaged elements according to the interlaminar failure criterion of Brewer and Lagacé (7); in yellow, damaged elements according to the intralaminar criterion (6).

Table 1: Setting of field variables according to the material state.

Material state	Stiffness	`FV1`	`FV2`
No failure	100%	0	0
Interlaminar failure (due to $\sigma_{rr}, \sigma_{r\theta}$)	5%	1	0
Intralaminar failure (due to $\sigma_{\theta\theta}$)	5%	0	1

Figure 1

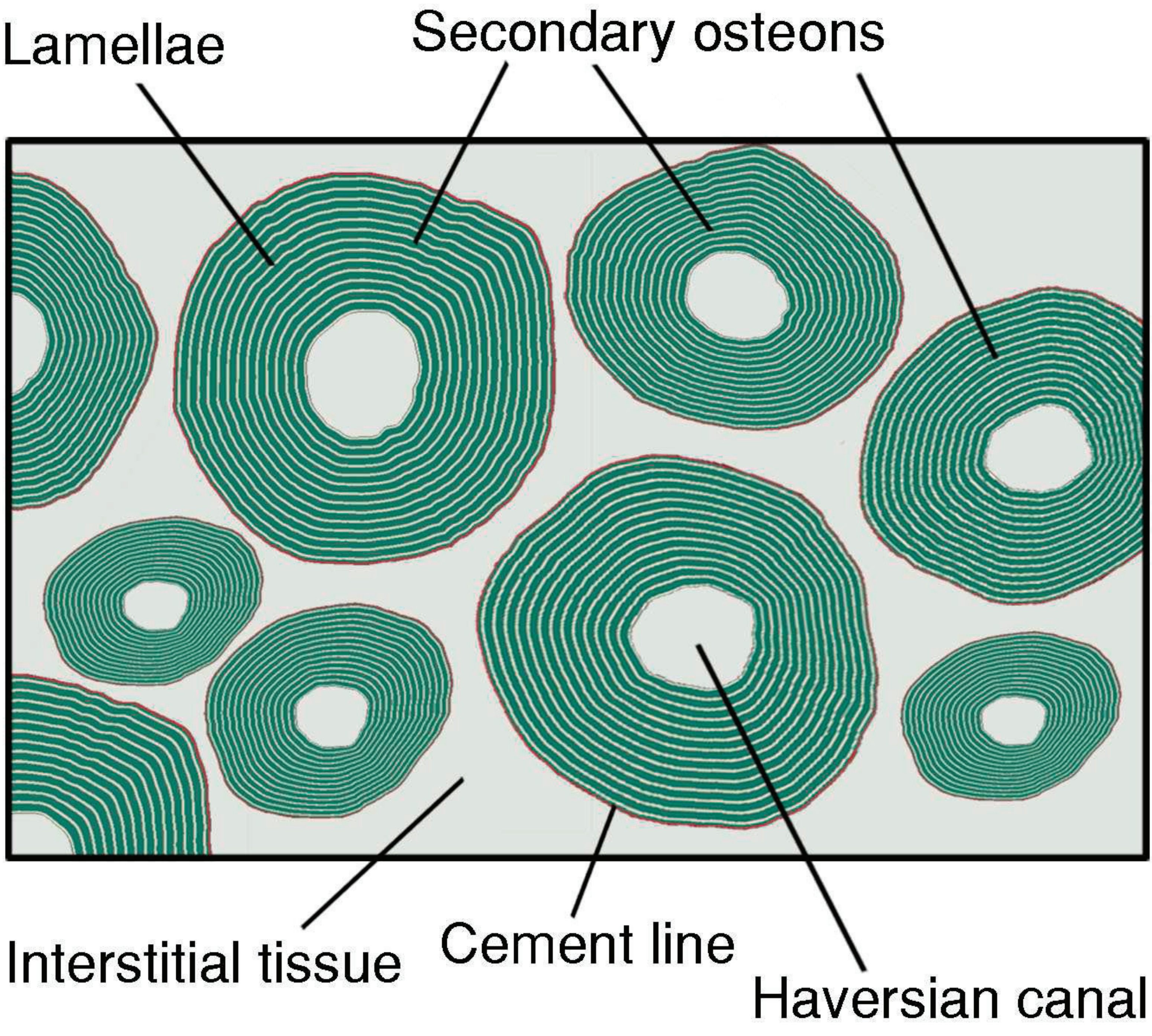
Lamellae
Secondary osteons
Interstitial tissue
Cement line
Haversian canal

Figure 2

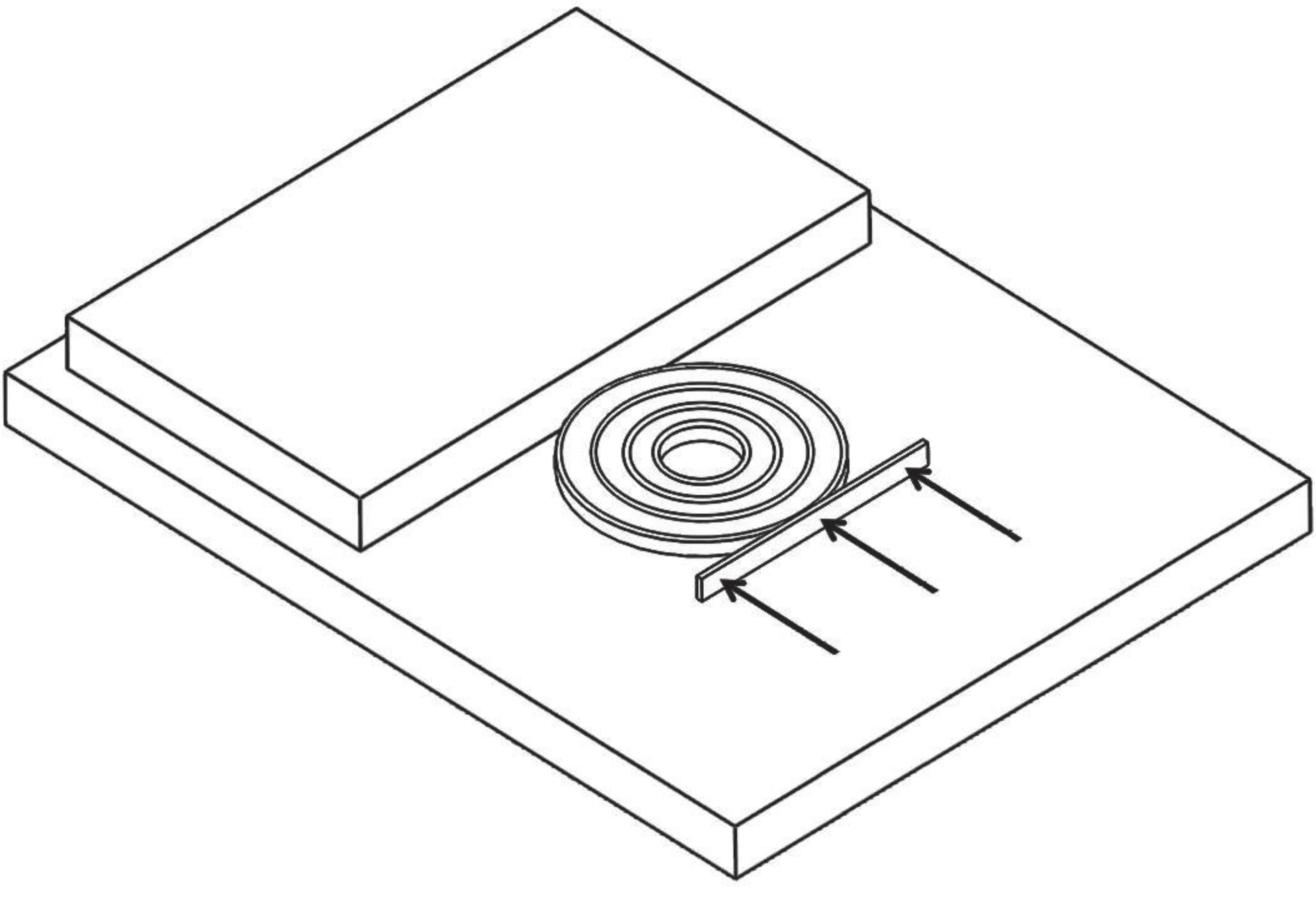

Figure 3

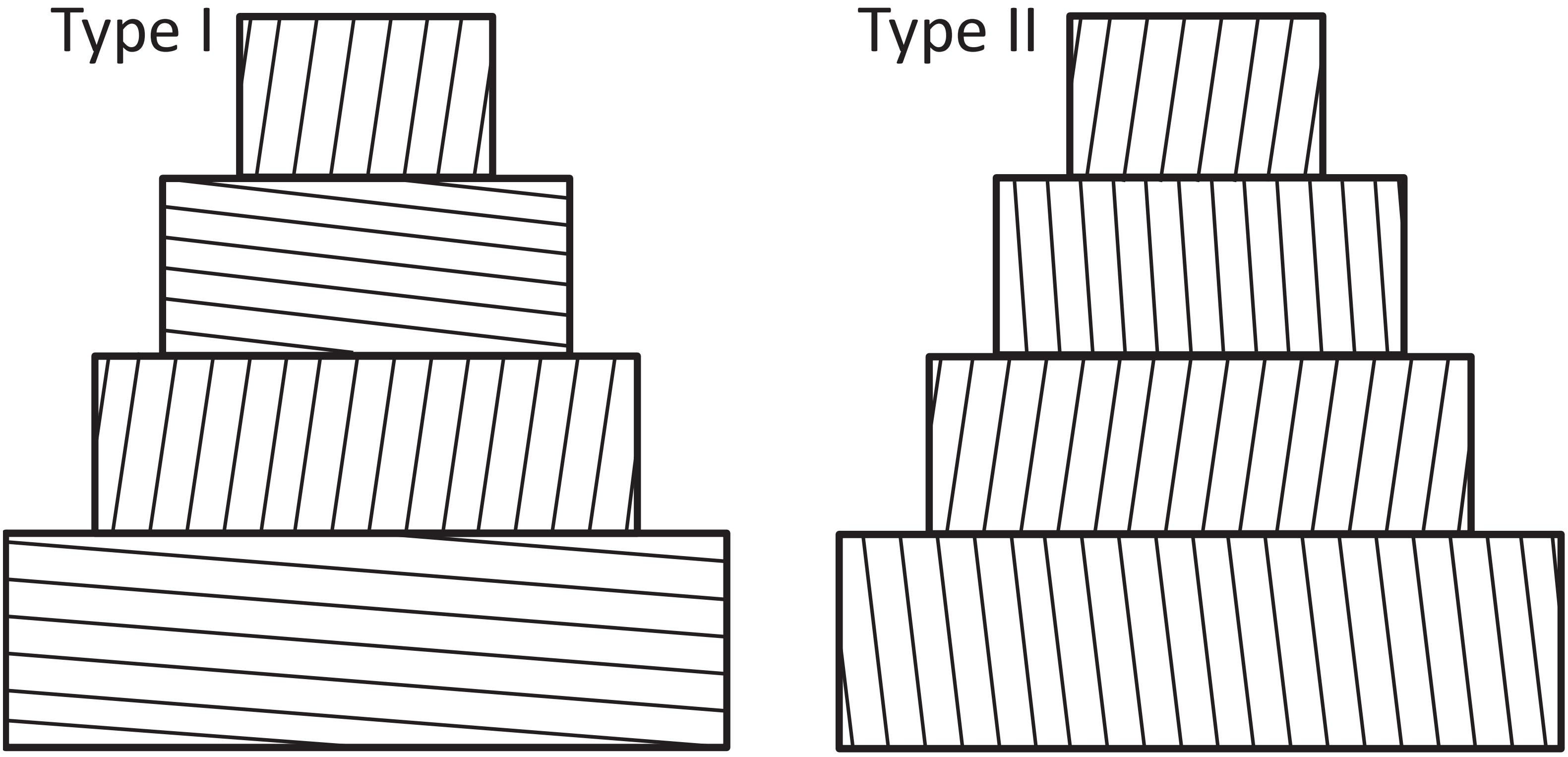

Figure 4

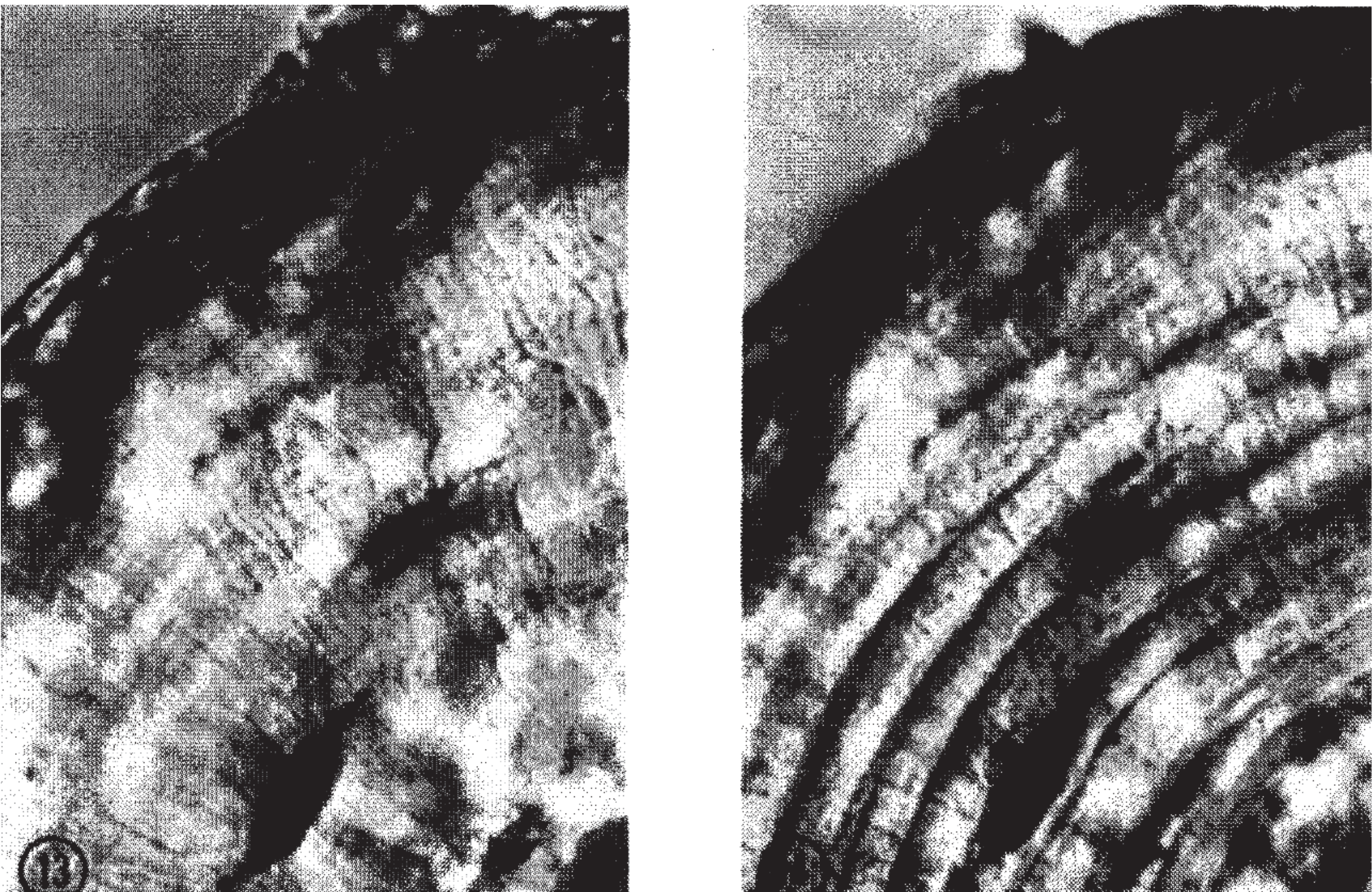

Figure 5

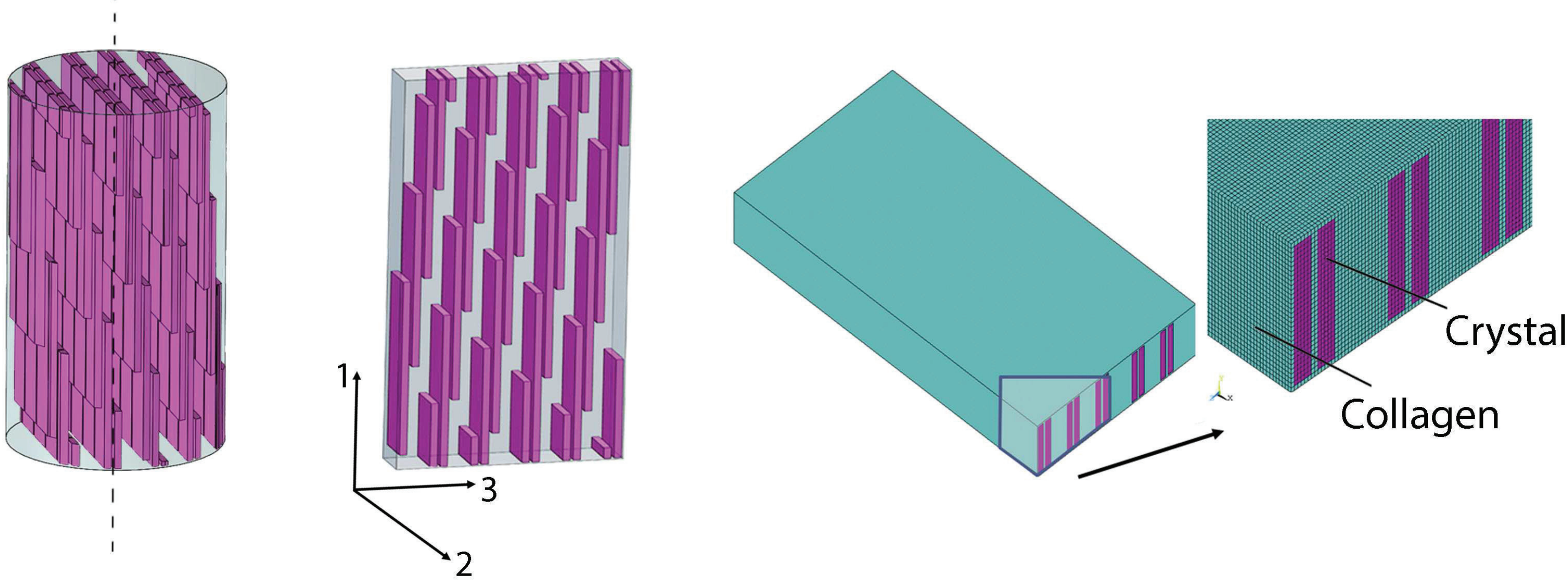

Figure 6

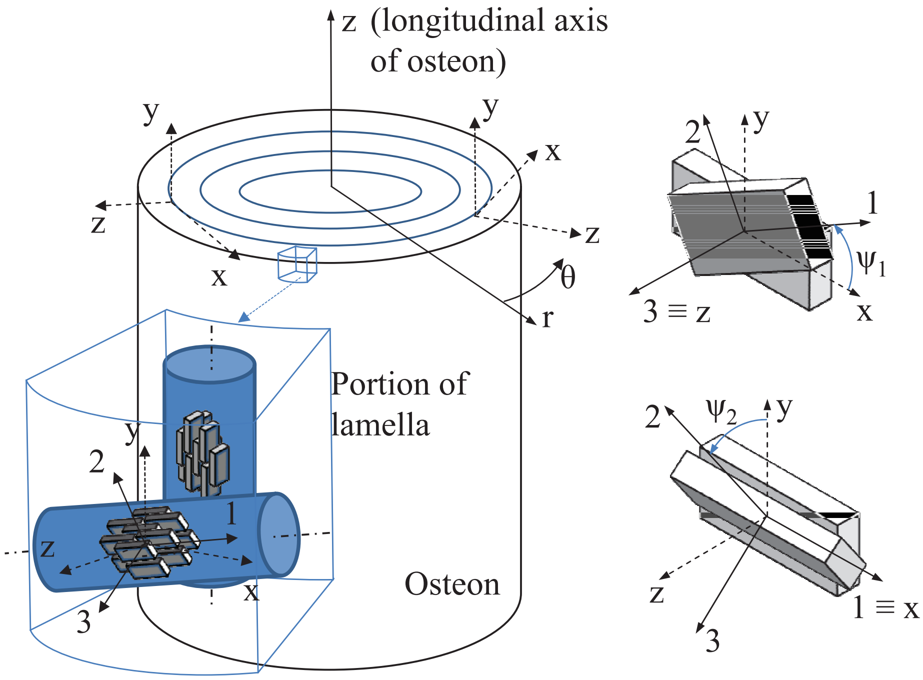
z (longitudinal axis
of osteon)
y
y
x
z
z
x
θ
r
Portion of
lamella
Osteon
y
2
1
z
x
3
2
y
1
ψ1
3 ≡ z
x
2
ψ2
y
z
1 ≡ x
3

Figure 7

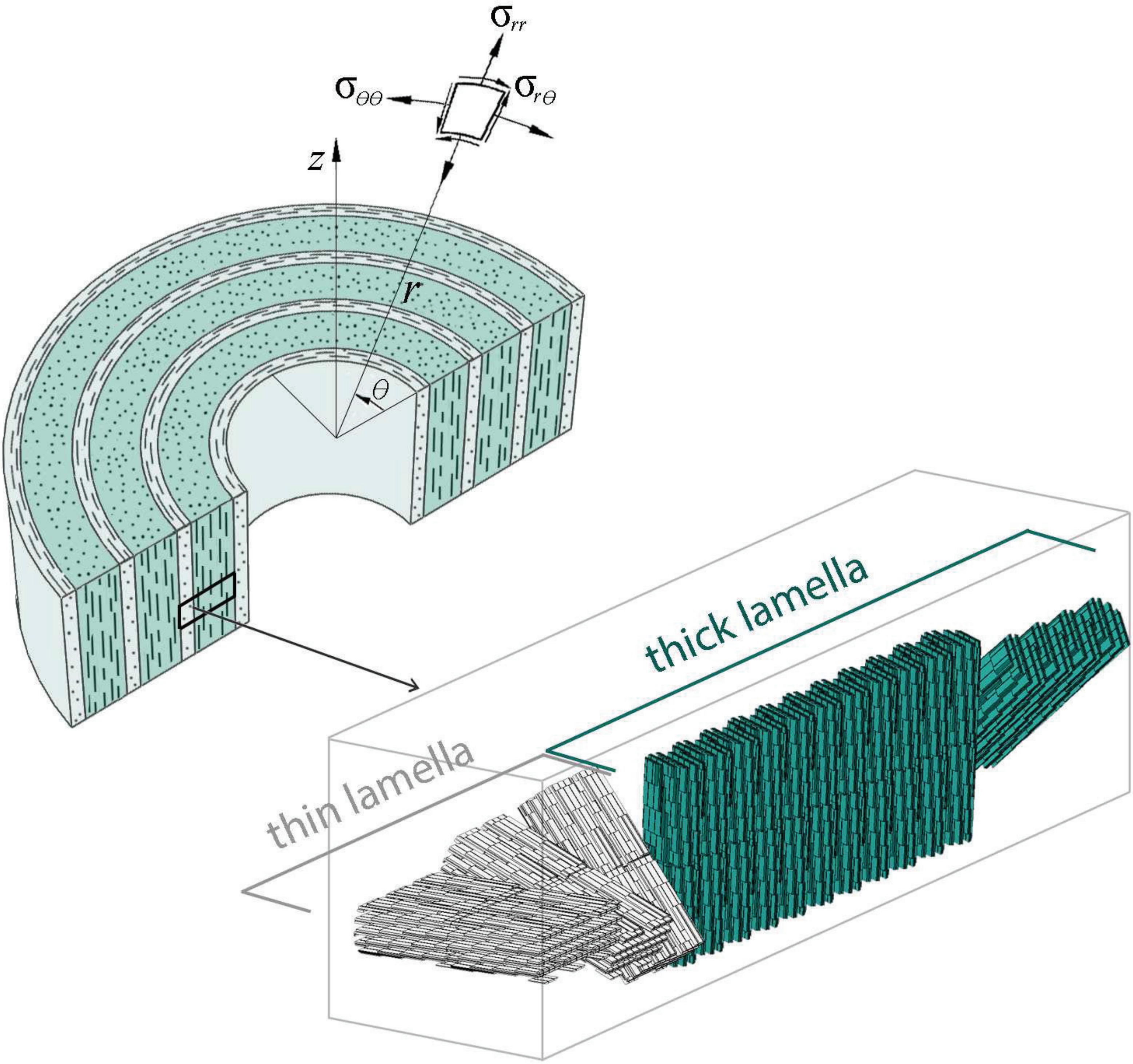

Figure 8

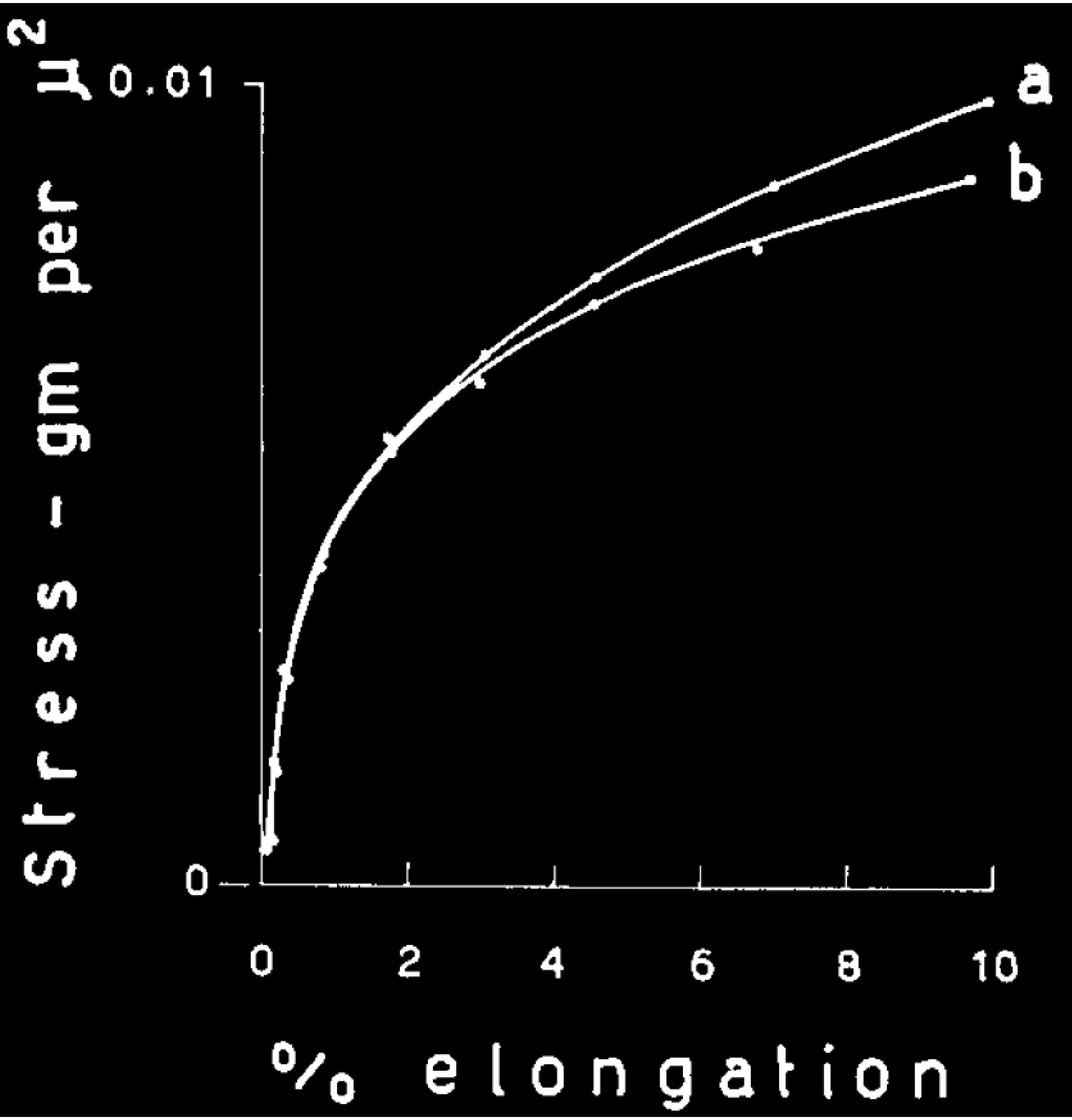

Figure 9

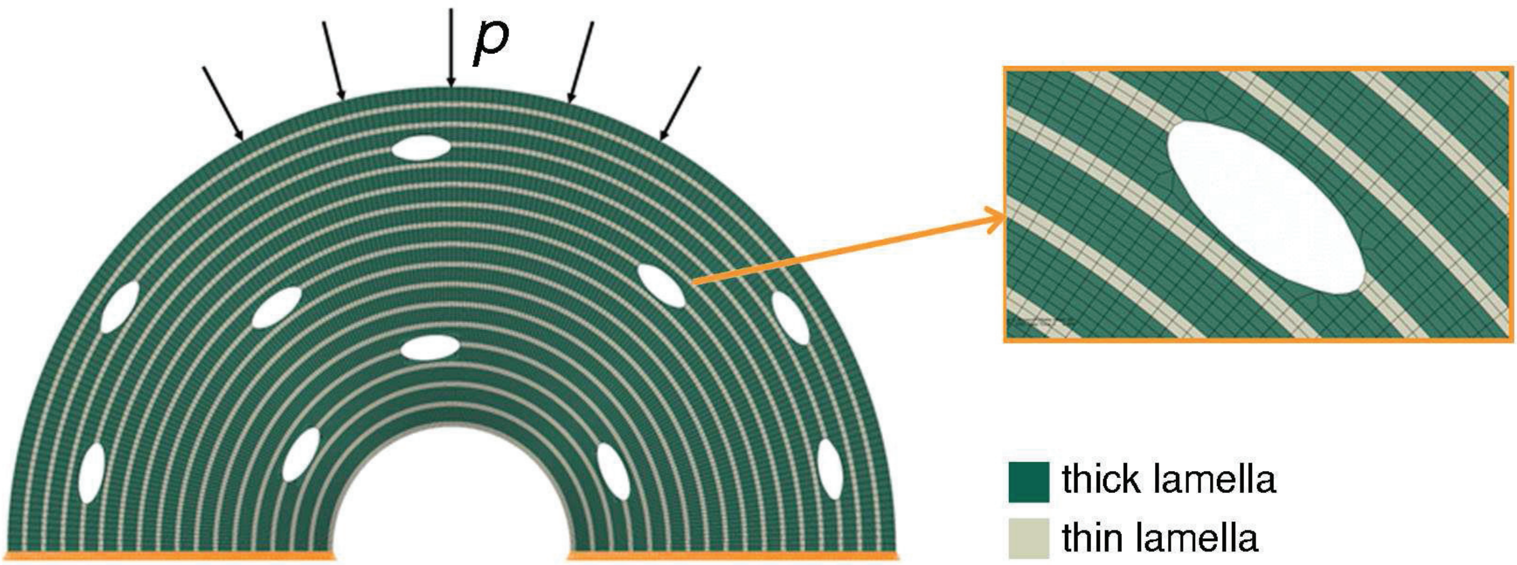

Figure 10

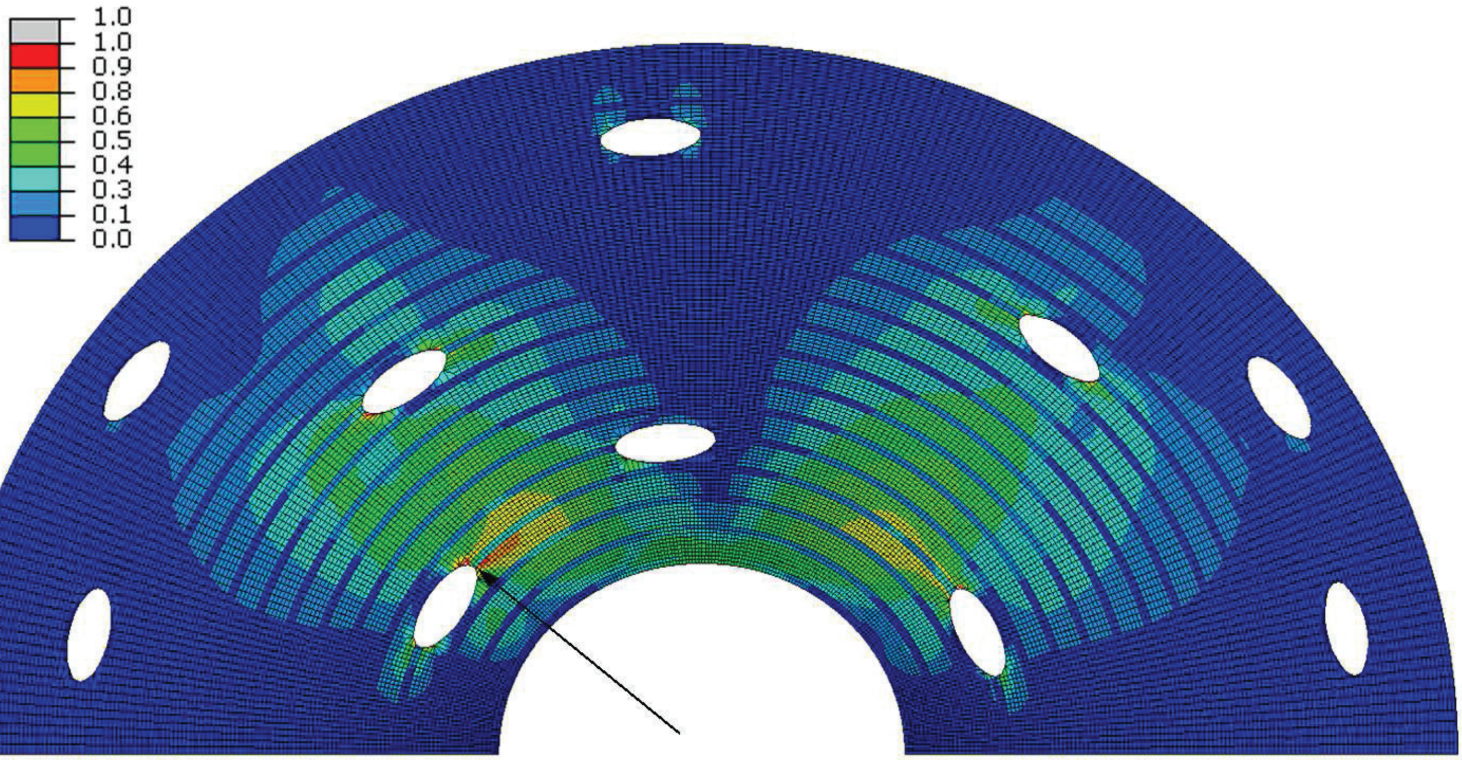

Figure 11

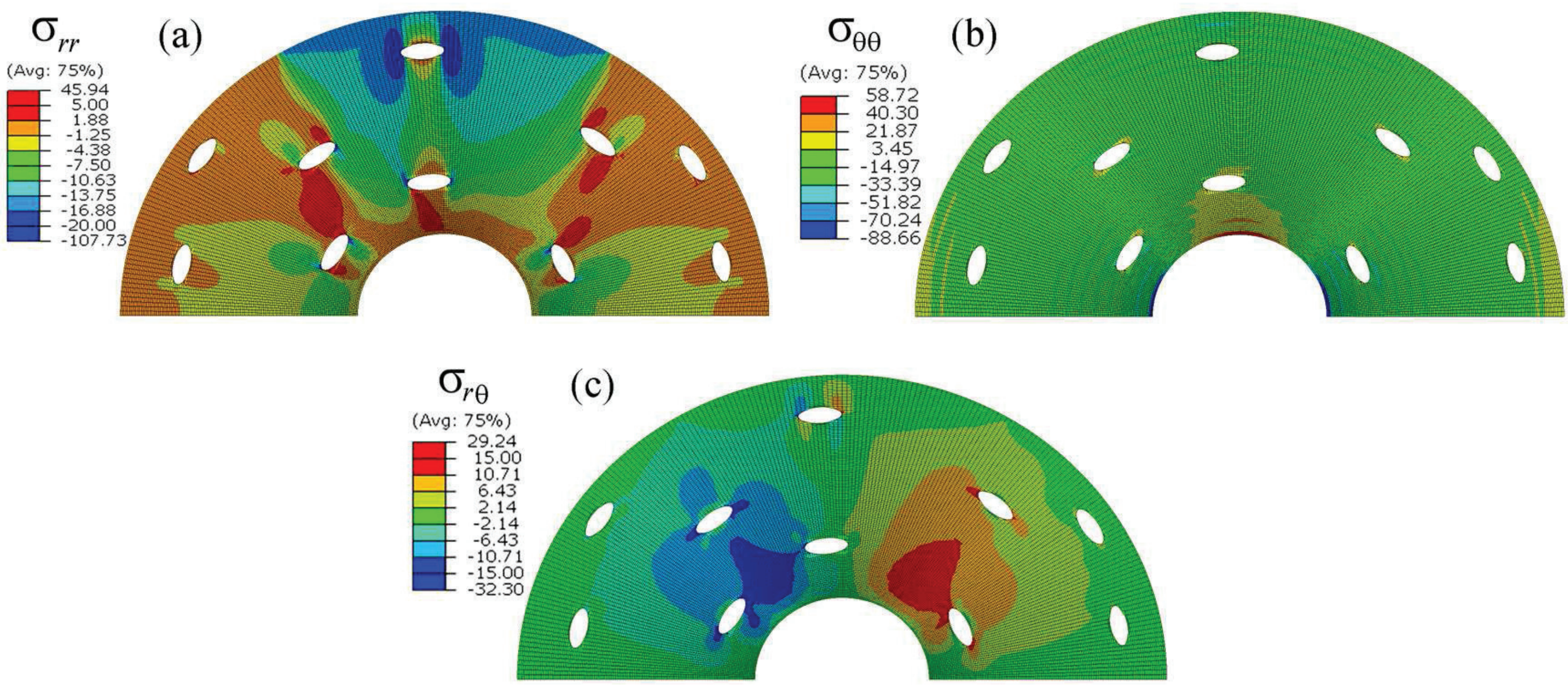

σrr
(a)
(Avg: 75%)
45.94
5.00
1.88
-1.25
-4.38
-7.50
-10.63
-13.75
-16.88
-20.00
-107.73
σθθ
(b)
(Avg: 75%)
58.72
40.30
21.87
3.45
-14.97
-33.39
-51.82
-70.24
-88.66
σrθ
(c)
(Avg: 75%)
29.24
15.00
10.71
6.43
2.14
-2.14
-6.43
-10.71
-15.00
-32.30

Figure 12

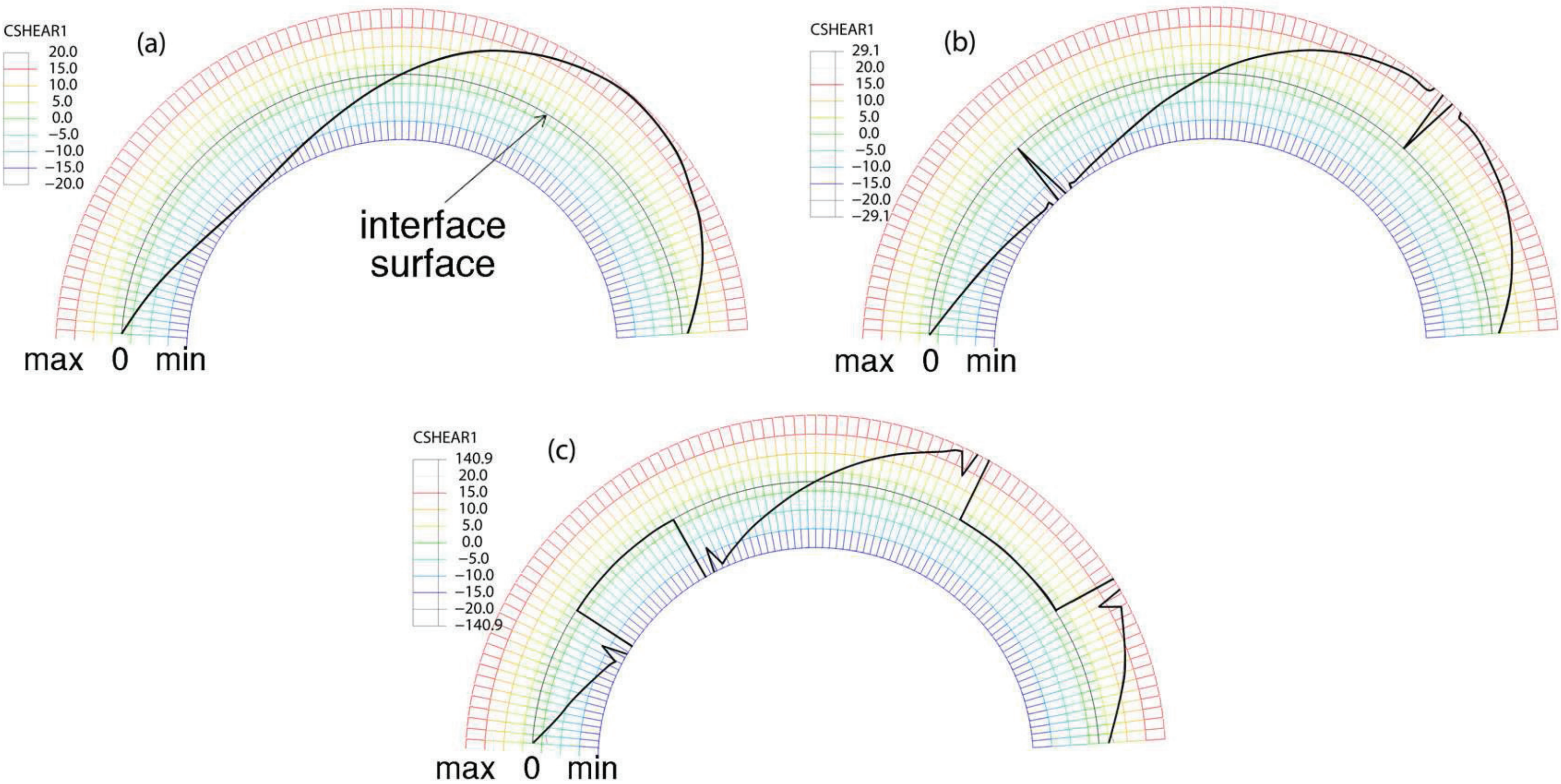

CSHEAR1
20.0
15.0
10.0
5.0
0.0
−5.0
−10.0
−15.0
−20.0
(a)
interface surface
max 0 min
CSHEAR1
29.1
20.0
15.0
10.0
5.0
0.0
−5.0
−10.0
−15.0
−20.0
−29.1
(b)
max 0 min
CSHEAR1
140.9
20.0
15.0
10.0
5.0
0.0
−5.0
−10.0
−15.0
−20.0
−140.9
(c)
max 0 min

Figure 13

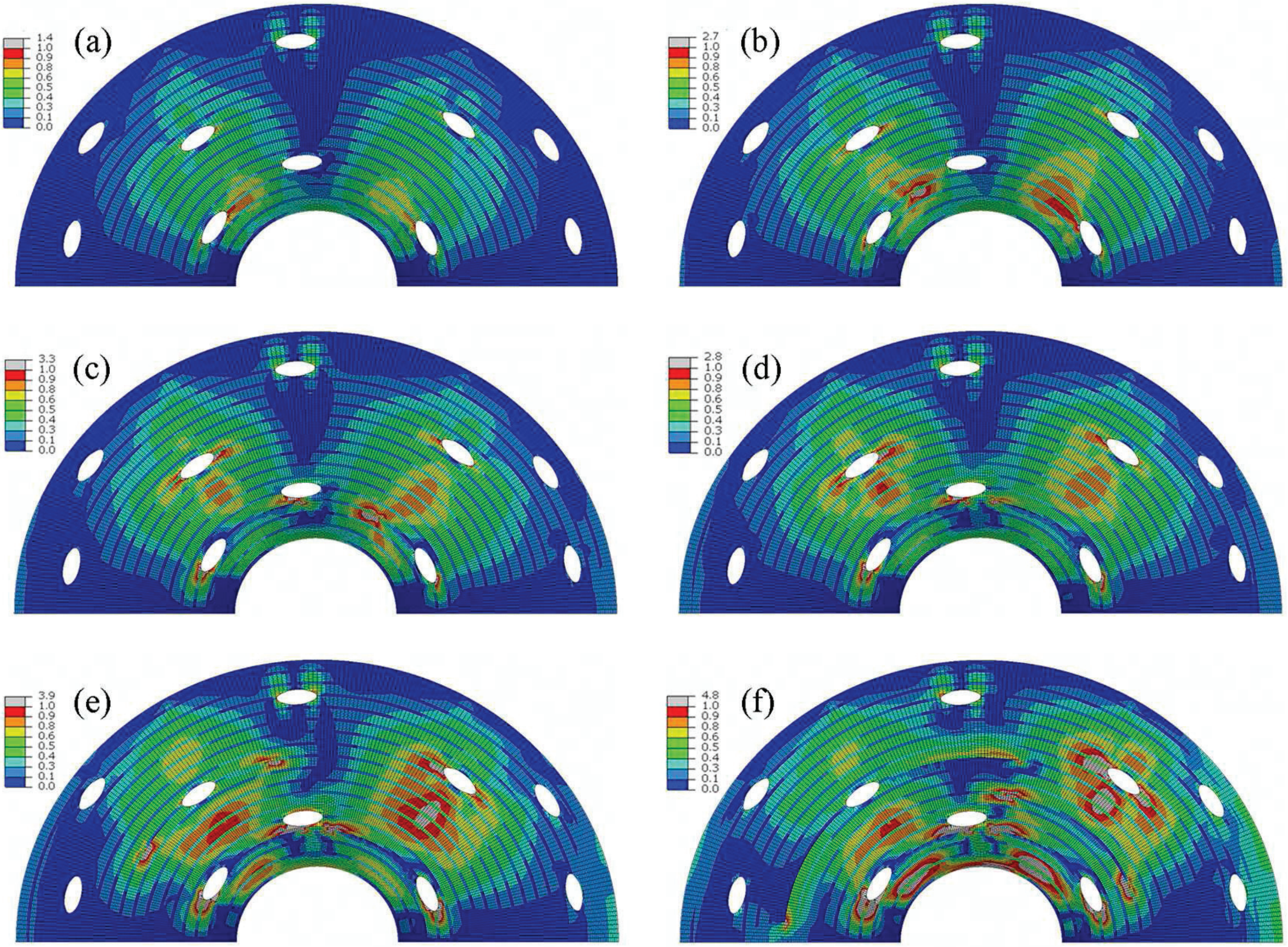
(a)
1.4
1.0
0.9
0.8
0.6
0.5
0.4
0.3
0.1
0.0
(b)
2.7
1.0
0.9
0.8
0.6
0.5
0.4
0.3
0.1
0.0
(c)
3.3
1.0
0.9
0.8
0.6
0.5
0.4
0.3
0.1
0.0
(d)
2.8
1.0
0.9
0.8
0.6
0.5
0.4
0.3
0.1
0.0
(e)
3.9
1.0
0.9
0.8
0.6
0.5
0.4
0.3
0.1
0.0
(f)
4.8
1.0
0.9
0.8
0.6
0.5
0.4
0.3
0.1
0.0

Figure 14

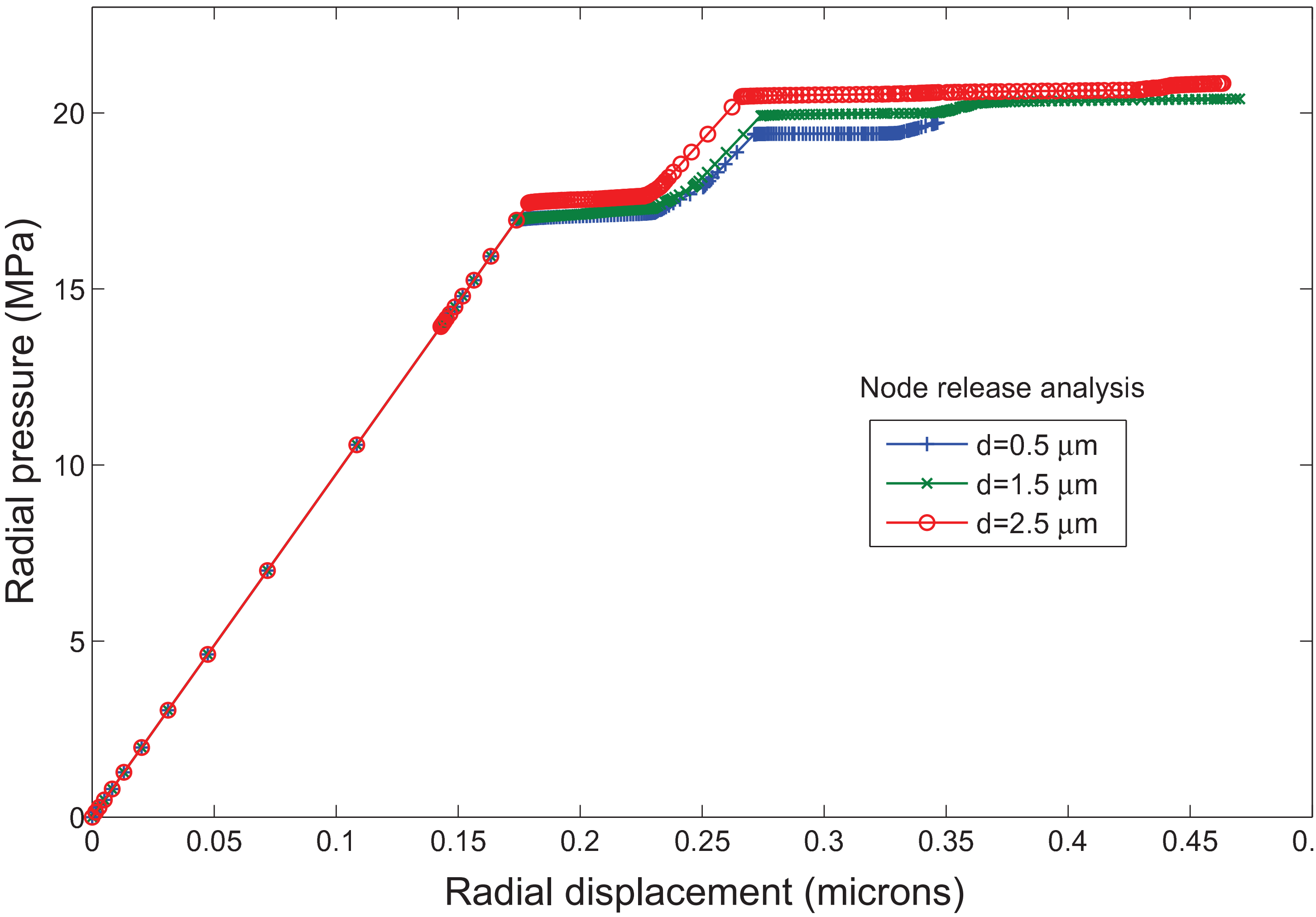

Node release analysis
d=0.5 μm
d=1.5 μm
d=2.5 μm
Radial pressure (MPa)
Radial displacement (microns)
0
5
10
15
20
0
0.05
0.1
0.15
0.2
0.25
0.3
0.35
0.4
0.45
0.5

Figure 15

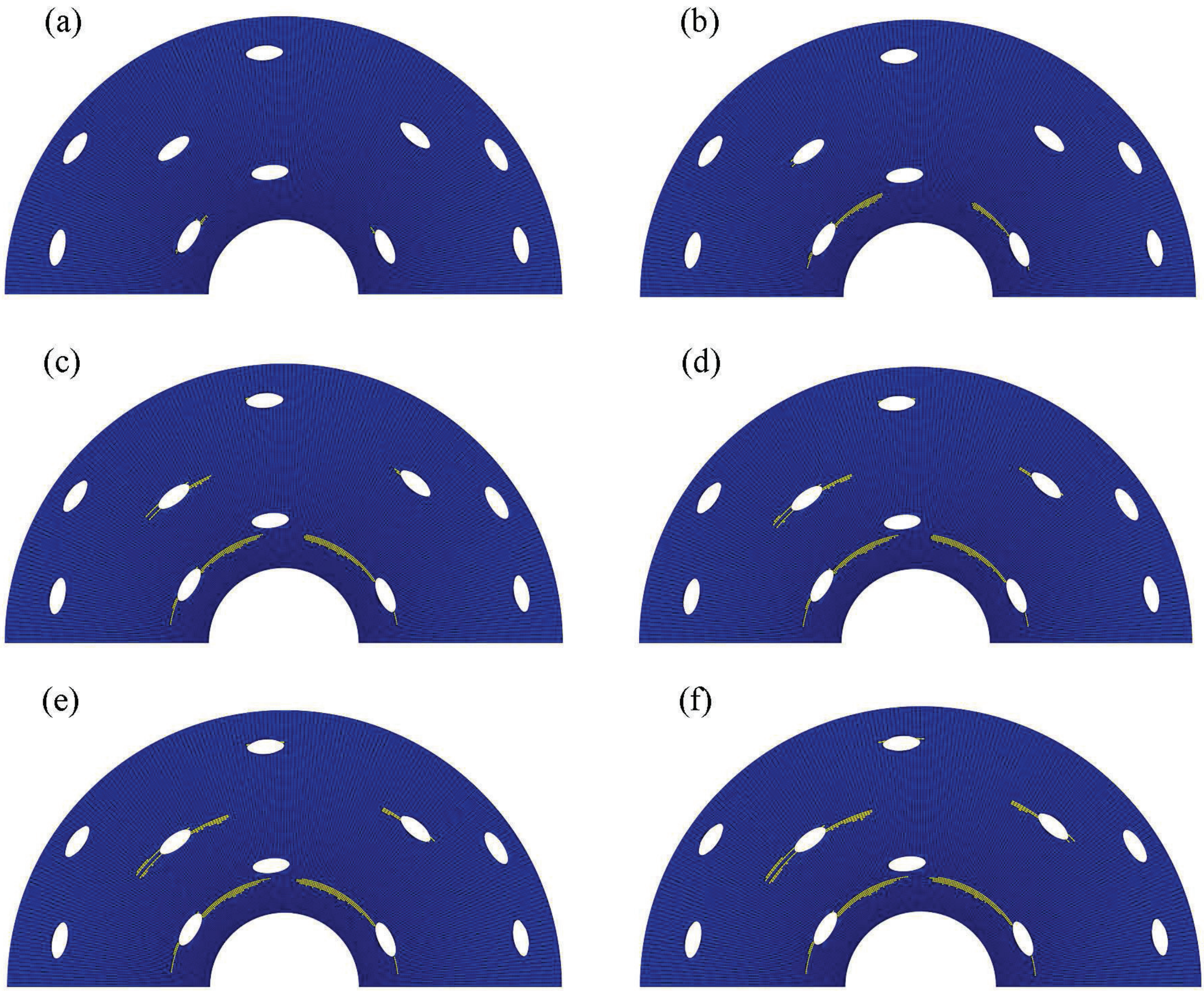

Figure 16

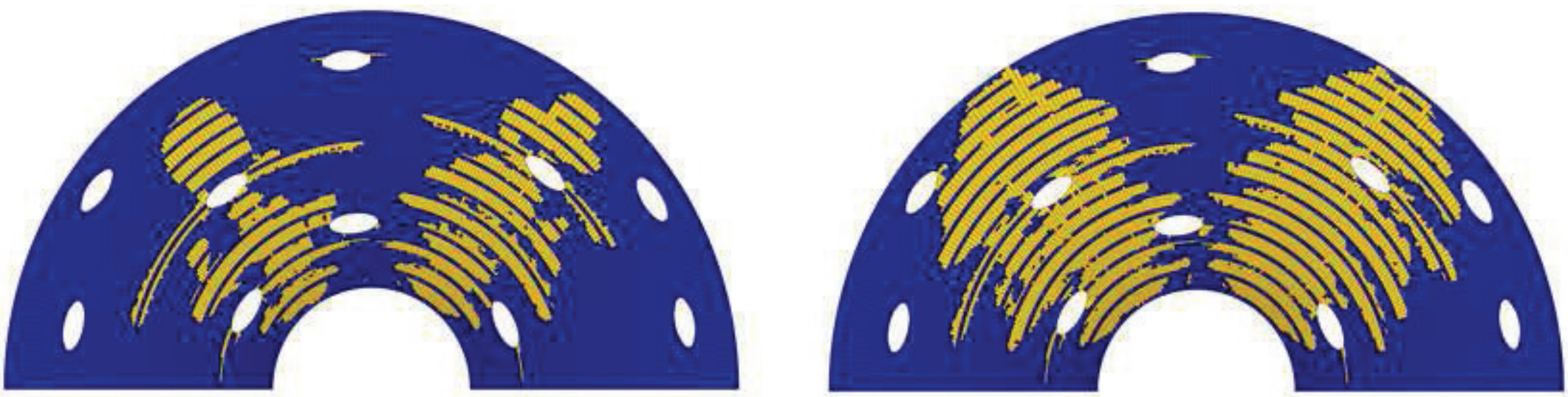

Figure 17

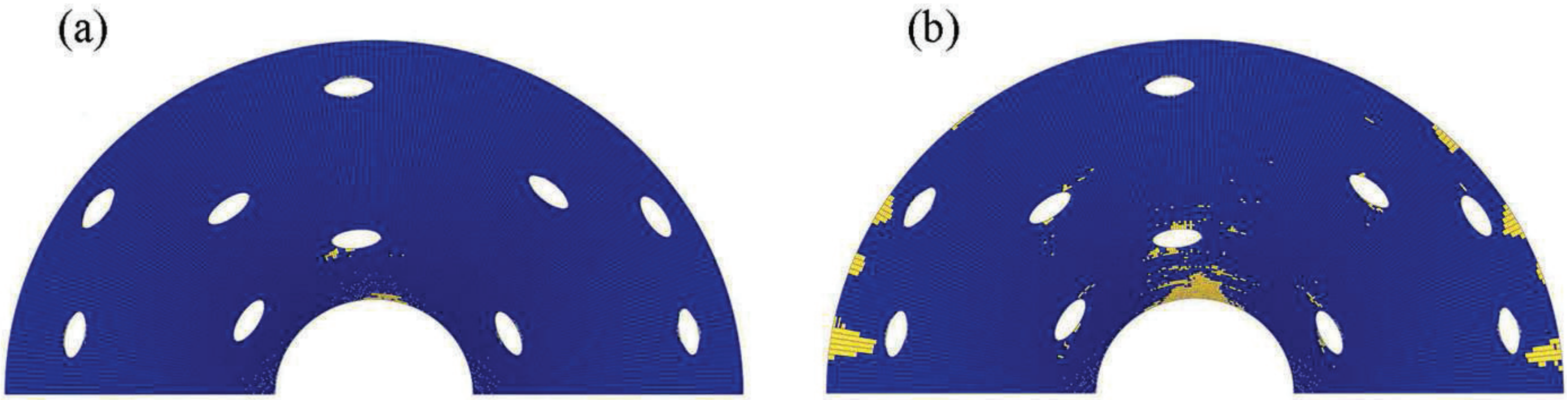

Figure 18

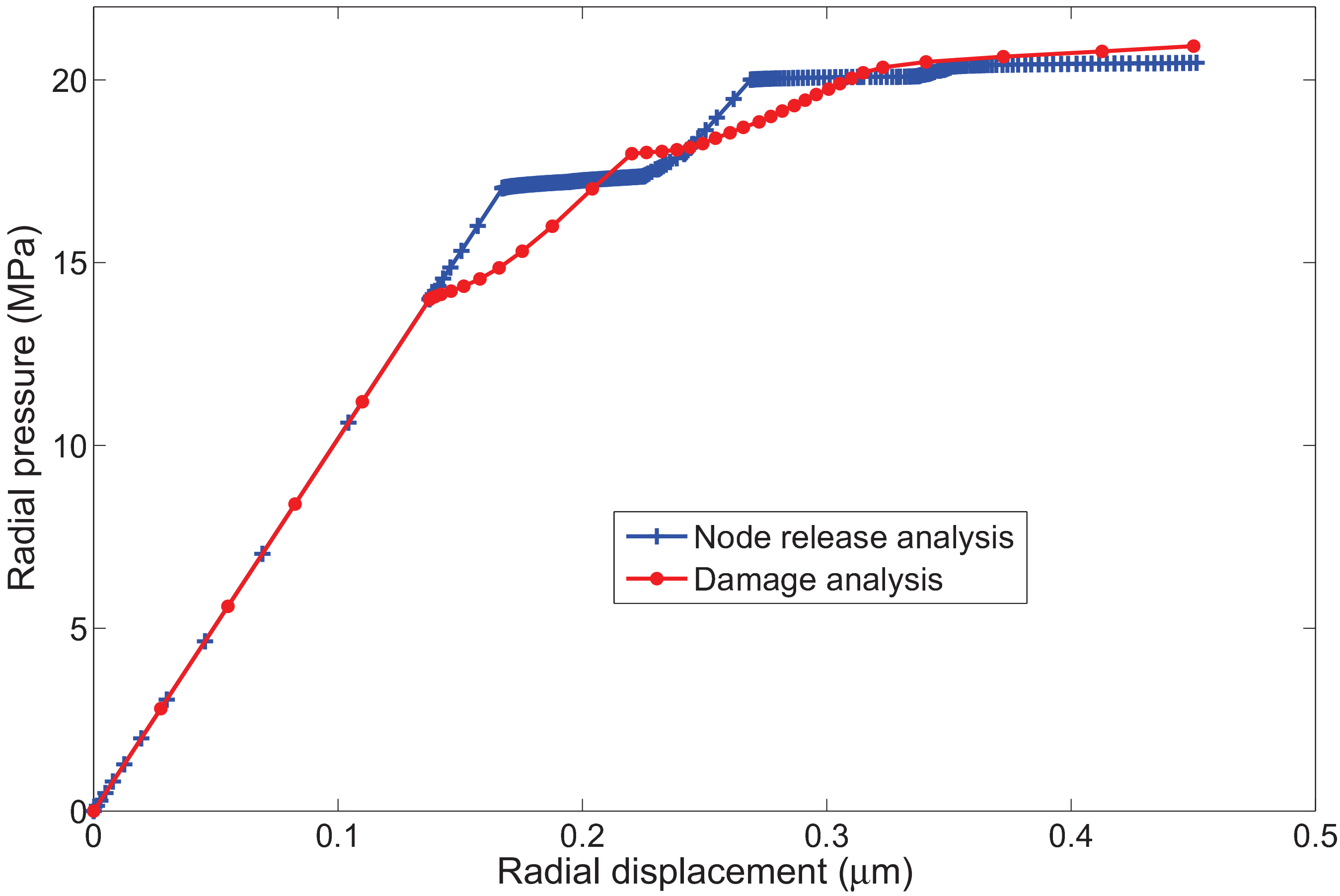
Radial pressure (MPa)
Radial displacement (μm)
Node release analysis
Damage analysis
0
5
10
15
20
0
0.1
0.2
0.3
0.4
0.5

Figure 19

(a) (b) (c)

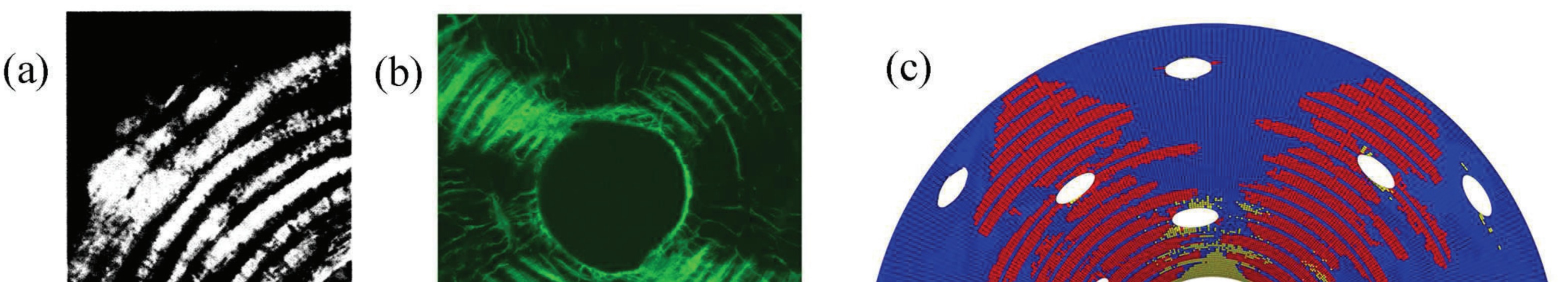

Table 1

Material state	Stiffness	FV1	FV2
No failure	100%	0	0
Interlaminar failure (due to $\sigma_{rr}, \sigma_{r\theta}$)	5%	1	0
Intralaminar failure (due to $\sigma_{\theta\theta}$)	5%	0	1